

Thermophile 90S Pre-ribosome Structures Reveal the Reverse Order of Co-transcriptional 18S rRNA Subdomain Integration

Jingdong Cheng^{1,3}, Jochen Baßler^{2,3}, Paulina Fischer^{2,3}, Benjamin Lau², Nikola Kellner², Ruth Kunze², Sabine Griesel², Martina Kallas², Otto Berninghausen¹, Daniela Strauss², Roland Beckmann^{1,*} and Ed Hurt^{2,*}

¹Gene Center, Department of Biochemistry and Center for integrated Protein Science Munich (CiPSM), Ludwig-Maximilians-Universität München, Feodor-Lynen-Strasse 25, 81377 Munich, Germany

²BZH, University of Heidelberg, Im Neuenheimer Feld 328, 69120 Heidelberg, Germany

³These authors contributed equally

*Correspondence: ed.hurt@bzh.uni-heidelberg.de, beckmann@genzentrum.lmu.de

SUMMARY

The 'birth' of the eukaryotic ribosome is preceded by RNA folding and processing reactions that depend on assembly factors and snoRNAs. The 90S (SSU-processome) is the earliest pre-ribosome structurally analyzed, which was suggested to assemble stepwise along the growing pre-rRNA from 5'>3', but this directionality may not be accurate. Here, by analyzing the structure of series of novel 90S assembly intermediates isolated from *Chaetomium thermophilum*, we discover a reverse order of 18S rRNA subdomain incorporation. This revealed that large parts of the 18S rRNA 3' and central domains assemble first into the 90S, before the 5' domain is stably integrated. This final incorporation depends on a physical contact between a heterotrimer Enp2-Bfr2-Lcp1 recruited to the flexible 5' domain and Kre33, which reconstitutes the Kre33-Enp-Bfr2-Lcp5 module on the compacted 90S pre-ribosome. Keeping the 5' domain temporarily segregated from the 90S scaffold could provide an extra time to complete the multifaceted 5' domain folding, which depends on a distinct set of snoRNAs and processing factors.

INTRODUCTION

Eukaryotic ribosome formation is the result of a cascade of interdependent assembly steps, during which the ribosomal RNA (rRNA) is synthesized, modified, processed and assembled with approximately 80 ribosomal proteins (r-proteins). Initially, the 18S, 5.8S and 25/28S rRNA are made as parts of a larger precursor (35S pre-rRNA in yeast) that is co-transcriptionally targeted at multiple sites by small nucleolar ribonucleoproteins (snoRNPs) for RNA modification, folded stepwise and decorated with r-proteins. These reactions are tightly coordinated by a large set of ribosome assembly factors (AFs), which transiently interact with the nascent rRNA and/or r-proteins to form the first pre-ribosomal particles. During the subsequent steps, compaction of the various rRNA subdomains and remodeling continues, which is coupled to rRNA processing reactions, leading to the sequential removal of the external (5'-ETS and 3'-ETS) and internal (ITS1 and ITS2) transcribed spacers. Further on in the assembly pathway, the pre-ribosomal subunits relocate from the nucleolus to the cytoplasm, where final maturation and proof-reading generates mature ribosomal subunits (reviewed in (Bassler and Hurt, 2018; Klinge and Woolford, 2018).

An early assembly intermediate formed during eukaryotic ribosome synthesis is the 90S pre-ribosome (also referred to as the SSU processome), the structure of which has been recently revealed by cryo-EM using particles from both the thermophilic fungus *Chaetomium thermophilum* and baker's yeast *Saccharomyces cerevisiae* (Barandun et al., 2018; Chaker-Margot et al., 2017; Cheng et al., 2017; Kornprobst et al., 2016; Sun et al., 2017). Typically, these 90S particles exhibit a near to mature 5' domain, a significantly formed central domain, and partially assembled 3' major and 3' minor domains (Barandun et al., 2018; Chaker-Margot et al., 2017; Cheng et al., 2017; Kornprobst et al., 2016; Sun et al., 2017). Importantly, these structures also revealed in pseudo-atomic detail how half a hundred of 90S factors, 15 r-proteins and the U3 snoRNP decorate the 5'-ETS and the nascent 18S rRNA.

A characteristic of the 90S pre-ribosome is that it contains many AFs modularly organized into biochemically stable subcomplexes (Bassler et al., 2017; Hunziker et al., 2016; Krogan et al., 2004; Perez-Fernandez et al., 2011; Perez-Fernandez et al., 2007; Pöll et al., 2014; Zhang et al., 2016a). Amongst

these modules is the UTP-A complex (Hunziker et al., 2016; Kornprobst et al., 2016; Pöll et al., 2014), which consists of seven structural proteins (Utp4, Utp5, Utp8, Utp10, Utp9, Utp15, and Utp17) that also chaperone the nascent 5'-ETS as it emerges from the transcribing RNA polymerase I (Gallagher et al., 2004; Hunziker et al., 2016; Kornprobst et al., 2016; Perez-Fernandez et al., 2007). A second module that also binds to the 5'-ETS rRNA is UTP-B (Utp1, Utp6, Utp12, Utp13, Utp18, and Utp21), which, like UTP-A, predominantly consists of a coating structural β -propeller combined with α -helical domains (Hunziker et al., 2016; Kornprobst et al., 2016; Pöll et al., 2014; Zhang et al., 2016a). Another prominent module is the U3 snoRNP (U3 snoRNA, Nop1, Nop58, Nop56, Snu13, Rrp9), which, after binding with the other modules, constitutes the 5'-ETS particle that serves as a structural platform for further constructing the various 18S rRNA subdomains until the biochemically stable 90S is formed (Barandun et al., 2018; Chaker-Margot et al., 2017; Cheng et al., 2017; Kornprobst et al., 2016; Sun et al., 2017). During these later assembly steps, other 90S AFs join the nascent 90S, including the Mpp10 complex (Mpp10–Imp3–Imp4–Utp3/Sas1) ((Granneman et al., 2003; Sa-Moura et al., 2017) associated with the evolving 3' major domain, the UTP-C complex (Utp22–Rrp7) ((Lin et al., 2013; Perez-Fernandez et al., 2007) located at the central domain, the Bms1–Rcl1 heterodimer (Delprato et al., 2014; Wegierski et al., 2001) positioned in the rRNA 5' domain region, and Bfr2–Enp2 (Soltanieh et al., 2014); the latter, however, is only partially visible in the recent EM structures (Barandun et al., 2018; Chaker-Margot et al., 2017; Cheng et al., 2017; Kornprobst et al., 2016; Sun et al., 2017). Based on these structural insights and further studies in yeast, in which 3'-truncated pre-rRNA fragments of various length were expressed and affinity purified, followed by identification of associated AFs (Chaker-Margot et al., 2015; Zhang et al., 2016b), a model of temporal 90S assembly was proposed. Accordingly, the SSU processome is assembled in a 5' to 3' direction with the co-transcriptional construction of the 40S subunit within the 90S scaffold. Thus, the temporal folding of the typical 18S rRNA subdomains (5' domain, central domain, 3' major domain, 3' minor domain) as they exist in mature 40S subunits was shown to be coupled with the timely recruitment of the distinct AFs and modules described above (Barandun et al., 2018; Klinge and Woolford, 2018).

In this study, we identified new 90S modules, based on reconstitution of *Chaetomium thermophilum* ribosome AFs, which often have superior biochemical properties compared to their mesophilic counterparts (e.g. from yeast). The two modules under investigation, the NocNop14–Emg1–Enp1–Rrp12 and Kre33–Enp2–Bfr2–Lcp5 complexes, were subsequently assigned in novel cryo-EM structures of 90S pre-ribosomes isolated using a split-tag affinity-purification method simultaneously established in the thermophile. Based on these new insights, we performed a structure-based mutagenesis of the Kre33 module members in yeast, which revealed their essential role in the early steps of 90S assembly. However, in contrast to the current working models, we found that 90S assembly does not follow a strict 5'→3' co-transcriptional direction. Instead it is the 5' rRNA domain that is the latest one to be stably incorporated in the 90 pre-ribosome.

RESULTS

Identification of New 90S Modules Based on Biochemical Reconstitution of Thermophilic Ribosome Assembly Factors

To specify the ribosome AF network on the 90S pre-ribosome, we focused on two-hybrid interactions previously identified between *Chaetomium thermophilum* AFs ([Bassler et al., 2017](#)), with the goal to reconstitute them into biochemically stable modules. A strong two-hybrid pair was detected between *ctKre33* helicase/acetyltransferase and *ctBfr2*. Since human Bfr2 (AATF) is part of a trimeric AATF–NGDN–NOL10 (ANN) complex ([Bammert et al., 2016](#)), we performed additional two-hybrid analysis with *ctEnp2* (human NOL10) and *ctLcp5* (human NGDN). Accordingly, the two-hybrid network around these factors could be expanded, demonstrating that *ctKre33* interacts with both *ctBfr2* and *ctEnp2*; however, *ctLcp5* interacts with *ctBfr2* but with neither *ctKre33* nor *ctEnp2* ([Figure S1A](#)).

A further set of two-hybrid data pointed to a second cluster of 90S factors including *ctNop14/Utp2*, *ctNoc4/Utp19*, *ctEmg1* and *ctEnp1*, all of which are located in a similar area of the 90S pre-ribosome ([Barandun et al., 2017](#); [Cheng](#)

et al., 2017). We also considered *ctRrp12* to be part of this cluster, based on a two-hybrid interaction found between *ctEnp1* and C-terminally tagged *ctRrp12* (Figure S1A).

To verify these two two-hybrid clusters by biochemical reconstitution, the implicated *ct90S* factors were recombinantly expressed in yeast and tested for assembly into complexes, based on a split-tag affinity purification strategy. Regarding the AFs linked to Kre33, it was possible to reconstitute dimers of *ctKre33-ctEnp2*, *ctKre33-ctBfr2*, *ctBfr2-ctEnp2*, and *ctBfr2-ctLcp5*, but no direct interaction between *ctLcp5* and *ctKre33* or *ctEnp2* was found, consistent with the two-hybrid data. Moreover, a trimeric *ctEnp2-ctBfr2-ctLcp5* complex, and a tetrameric *ctKre33-ctEnp2-ctBfr2-ctLcp5* complex (referred to as the "Kre33 module"), could be isolated (Figure 1A and S1B).

Regarding the Nop14 linked factors, we were able to reconstitute the dimeric complexes *ctNoc4-ctNop14* ((Kuhn et al., 2009), *ctNop14-ctEmg1* ((Liu and Thiele, 2001), *ctRrp12-ctEmg1*, and *ctRrp12-ctEnp1*. Furthermore, trimeric *ctNoc4-ctNop14-ctEmg1*, tetrameric *ctNoc4-ctNop14-ctEmg1-ctRrp12*, and pentameric *ctNoc4-ctNop14-ctEmg1-ctRrp12-ctEnp1* complexes could be isolated (Figure 1B and Figure S1B). In the case of *ctRrp12*, the N-terminal heat-repeat domain (residues 1–1039) was used in the reconstitution studies, which exhibited better biochemical properties than the full-length protein. However, the 189-residue Rrp12 C-terminal extension has important *in vivo* functions, since a *rrp12ΔC* yeast strain grew slowly, although Rrp12ΔC was still assembled into 90S particles (Figure S1C).

We conclude from this wealth of two-hybrid and biochemical data that in addition to the well-established 90S modules (i.e. UTP-A, UTP-B, UTP-C, U3 snoRNP, Mpp10 complex, Bms1-Rcl1), other subcomplexes exist that might perform specific, yet so far undefined, roles in 90S biogenesis.

Cryo-EM structure of Thermophile 90S Assembly Intermediates Co-enriched for Kre33 and Noc4 Modules

To visualize these newly identified modules on the 90S pre-ribosome, we sought to refine our *Chaetomium thermophilum* cryo-EM map (Cheng et al., 2017),

which only allowed assignment of Kre33 but not Enp2, Bfr2, or Lcp5, and in the case of the Noc4 module, only Noc4, Nop14, and Emg1, but not Enp1 or Rrp12. To gain further information by cryo-EM, we aimed isolating 90S particles from *Chaetomium thermophilum* by split-tag affinity purification, using *ctKre33* as first bait and *ctNoc4* as second, which was predicted to co-enrich both modules more efficiently.

A prerequisite for establishing such a split-tag affinity-purification method in *Chaetomium thermophilum* was the development of a second selectable marker working at high temperatures. For this purpose, we generated a thermostable hygromycin phosphotransferase based on the orthologous gene from the archaeon *Sulfolobus solfataricus* (Cannio et al., 2001), which indeed could be used as an additional selection marker (see Methods). In a next step, we coupled this hygromycin marker to the first bait (*ctKre33*) fused to the protein A tag including a TEV-cleavage site. After selection of hygromycin-resistant transformants expressing *ctKre33*-TEV-Prot A, this strain was transformed with a construct harboring the second bait, Flag-tagged *ctNoc4*, coupled to the already established *ERG1* selectable marker (Kellner et al., 2016). The obtained double transformants, expressing both protein-A-tagged Kre33 and Flag-tagged Noc4 under their endogenous promoters, were selected and subjected to split-tag affinity purification. This yielded the desired pre-ribosome preparation with the set of expected 90S factors, including Kre33–Enp2–Bfr2–Lcp5 and Noc4–Nop14–Emg1–Rrp12–Enp1 (Figure 1C and Table S1, sheet 1). We refer to this preparation as to the "*ctKre33-ctNoc4* 90S particle" that was subsequently used for cryo-EM analysis (Figure 1D; for particle sorting, see Figure S2)

Consistent with previous 90S structures, Kre33 is attached as a homodimer to the nascent 5' domain of the 18S rRNA in the "head" of the pre-90S particle (Figure 1D and 2A) (Barandun et al., 2017; Chaker-Margot et al., 2017; Cheng et al., 2017; Kornprobst et al., 2016; Sun et al., 2017). However, the new EM structure allowed proper building of the Kre33 module to include a more complete Kre33 dimer, Enp2, and Lcp5 in the head (see below). Moreover, the improved particle allowed us to assign and build the C terminus of Bfr2, which wraps around the Enp2 β -propeller (Figure 2A and B, see below). Furthermore,

we built large parts of the Noc4 module, including Noc4, the Emg1 dimer, and Nop14, which together bridge the "base" and "body" of the 90S particle (Figure 1D and Figure 2C). Finally, we could assign and position homology models for Rrp12, Enp1, eS12, and h34–39 of the 18S rRNA in the base of the 90S particle (Figure 2C and D) (Barandun et al., 2017; Cheng et al., 2017).

Sequential Incorporation of 18S rRNA Subdomains into the 90S Pre-ribosome

By using Kre33 incorporated in the head and Noc4 situated in the base of the 90S as baits for split-tag purification, we could successfully resolve a series of different *Chaetomium thermophilum* 90S pre-ribosome cryo-EM structures, all representing states before pre-rRNA A1 cleavage (Figure 3). Four of these intermediates, termed states A, B1, B2, and C, have a well incorporated platform of the pre-40S ribosome, and, in this respect, resemble the 90S structures previously described (Cheng et al., 2017; Kornprobst et al., 2016; Sun et al., 2017). However, two other 90S structures, termed state a and state b, contain the platform in an outward position (Figure 3), which has only been observed so far in the yeast 90S structure purified from starvation conditions (Barandun et al., 2017). All of the new 90S structures described here have a range of resolutions between 3.5 and 7.1 Å, which allowed for building and fitting molecular models (full models for states B1 and B2).

To our surprise, in state A and state a, the 5' domain of the pre-40S, which is the first to be transcribed by RNA Pol I after the 5'-ETS, is not yet incorporated into the 90S particle (Figure 3). Only h16 and h17, which are required for the binding of the Bms1 GTPase, could be observed, whereas the central, the 3' major, and 3' minor domains of the pre-18S were visible. At the same time, in state a, even the central domain is still in the outward position, kept in place by Rrp5 and the UTP-C complex. Moreover, taking the overall architecture of the 90S particles into account, it is apparent that stable incorporation of the pre-18S rRNA 5' domain is highly likely to require the 3' major domain to first stabilize the 5'-ETS sub-particle, in particular the Bms1 complex and the Kre33 module, for 5' domain interaction. This finding agrees well with previous data showing that both the Bms1 and the Kre33 subcomplexes require the 3' domains to be efficiently recruited to the 90S/SSU processome (Chaker-Margot et al., 2015; Zhang et al.,

2016b). Taken together, this data strongly supports the concept that the assembly of the pre-18S rRNA into the 90S particle starts with the 3' major and 3' minor domains to be first assembled with the 5'-ETS, which is later followed by incorporation of the pre-18S 5' domain and finally the platform (middle domain). Conceptually, this mirrors our previous observations on the pre-60S assembly pathway, in which domains I and II (5') interact with domain VI (3') before the sequential incorporation of the remaining domains (III, IV, V) into the maturing particle can occur (Kater et al., 2017).

First observed in state B1, the 5' domain and rRNA expansion segment 6 (ES6S) are stabilized on the 90S by Utp20 and the Kre33 module (Figure 3). Here, the submodule consisting of Enp2, Bfr2, and Lcp5 (Figures S2B) is connected to the pre-18S rRNA and hence is visible for the first time. When maturing into state B2, the UTP-C complex is incorporated into the 90S by binding to the platform of the pre-40S. Upon further maturation into state C, Utp30 dissociates, whereas the two r-proteins eS19 and eS27 are incorporated into the particle (Figure 4A and 4B). States a and b still have Rrp5 bound to the platform, whereas eS1 is absent. Together, this prevents further assembly of the central domain into the 90S particle and, moreover, it prevents the UTP-C complex progressing to state C. Thus, we speculate that state a represents an intermediate before state A, in which the assembly of pre-18S starts with only the 3' major and 3' minor domains, whereas association with both the central and 5' domains is yet to happen. In contrast, state b resembles the structure that was previously reported by the Klinge lab, when 90S particles were purified from starvation conditions (Barandun et al., 2017). Since in this state, Rrp5, which is sandwiched between UTP-C and the platform, prevents further maturation, it is difficult to assign its position in a thus far sequential assembly pathway observed under non-starving conditions. Hence, for the accumulated state b, growth regulating signals (e.g. TOR pathway, CURI complex, kinase activities; note that UTP-C is linked to the TOR pathway and CK2; (Albert et al., 2016) might be required to trigger continuation along the 90S maturation pathway.

UTP-C is Involved in Progression from 90S State B2 to C

The obvious changes taking place between states A/a and B/b is the transition of the 5' domain, from being delocalized to rigidly incorporated into the 90S particle, whereas the differences between state B and C are noted in two regions. One region is located around the UTP-C complex, consisting of Utp22 and Rrp7, which becomes incorporated into the 90S structure in state B2, contacting the tip of h44 as well as directly interacting with eS1 and Utp13. Upon further maturation into state C, r-protein eS27, which binds at the interface between rRNA h22 and h26, is positioned near and wrapped around by Rrp7. Thus, the UTP-C complex might be in a suitable position to establish a checkpoint here, for example, by ensuring that the 3' minor, central, and 5' domains are in the proper conformations for the next steps in the 90S maturation pathway, which are probably regulated and linked to other cellular pathways. The other region is around h41 and expansion segment ES10S of the pre18S rRNA, which in state B2 are retained by Utp30. Later, in state C, Utp30 dissociates, resulting in the correct folding of rRNA h41 and expansion segment ES10S. Moreover, this leads to the proper folding of the rRNA h42 and recruitment of the eS19 protein. As a result, this region is folded in a mature conformation and ready for interaction with rRNA h39.

Unusual Subunit Stoichiometry of the Kre33 Module on the 90S Pre-ribosome

Encouraged by these new structural data, in particular on the Kre33 module, we wanted to gain insight into its *in vivo* role, for which information is scarce. For this reason, we switched to *Saccharomyces cerevisiae* Kre33 and its binding partners, with the aim of exploiting the yeast genetic system for structure-based functional analyses. Individual affinity purifications of the tagged subunits scKre33, scEnp2, scBfr2 or scLcp5 demonstrated that they all co-enrich 90S particles, but the Kre33 module members were slightly over-stoichiometrically present compared to the other 90S AFs (Figure 5A). Upon separation of 90S particles from the free Kre33 module (purified using scEnp2-FTpA) by sucrose gradient centrifugation, both trimeric Enp2–Bfr2–Lcp5 and tetrameric Kre33–Enp2–Bfr2–Lcp5 complexes could be identified (Figure S3A). In contrast, affinity-

purified Kre33-FTpA, besides being associated with 90S particles, exhibited only the Kre33–Enp2–Bfr2–Lcp5 tetramer (Figure S3B and S3C).

After identification of the Kre33 module as a biochemical entity both in *Chaetomium thermophilum* and yeast, we queried the stoichiometry of the module members, since previous studies showed two adjacent Kre33 copies on the 90S cryo-EM structures (Figure 2B; (Barandun et al., 2017; Chaker-Margot et al., 2017; Cheng et al., 2017; Kornprobst et al., 2016). To investigate this, we determined the presence of a second protein copy for all four Kre33 module members on the 90S particles by an alternative method. For this purpose, each subunit was expressed in two different forms, one TAP-tagged to facilitate its affinity purification, and the other fused to GFP to discriminate between both forms. All four tagged bait proteins were functional, causing no apparent growth defects in yeast (data not shown), and capable of assembling into 90S pre-ribosomal particles (Figure 5A, Utp10-FTpA purification). However, upon affinity purification we noticed that only Kre33-ProtA co-precipitated the second Kre33-GFP copy, whereas Bfr2, Enp2, and Lcp5 did not co-enrich the corresponding GFP-tagged forms (Figure 5A). This data points to an unusual 2:1:1:1 stoichiometry for the Kre33–Enp2–Bfr2–Lcp5 module on the 90S pre-ribosome.

Thermophile 90S Cryo-EM Structure Explains the Yeast *kre33-1* Mutant

To shine light on the *in vivo* role of the Kre33 module for 90S biogenesis, we analyzed specific mutants in the yeast system. We began by engineering auxin-inducible yeast degron strains for Kre33, Enp2, and Bfr2, which allowed fast degradation of these factors with concomitant growth arrest (Figure S3D and S3E). All these depleted strains still could assemble 90S particles, but the transition from 90S to pre-40S particles was severely impaired (Figure 5B and 5C). 90S particles, isolated from either Bfr2- or Enp2-depleted cells, exhibited a strong reduction of the Enp2–Bfr2–Lcp5 core complex, but Kre33 was only partially absent (Figure 5D and Table S1, sheet 2 and 3). On the contrary, 90S particles isolated from the Kre33-depletion strain still contained normal levels of Enp2, Bfr2, and Lcp5 core (Figure 5D and Table S1, sheet 2 and 3). In all these depletion experiments, however, UTP-A, UTP-B, U3-snoRNP and Mpp10 modules, which together are joined in the 5' ETS particle (Kornprobst et al., 2016), did not significantly change, but the 90S factors associated with the 18S

moiety of the 90S (e.g. Noc4 module, UTP-C) became enriched (Figure 5D and Table S1, sheet 2 and 3). These findings led us to conclude that the Enp2–Bfr2–Lcp5 core complex is recruited to the 90S pre-ribosome independently of Kre33, but Kre33 itself exhibits a mixed targeting mechanism partly depending on the core Enp2–Bfr2–Lcp5. When considering also the structural insights, this data suggests that the stable incorporation of the 5' domain into the 90S depends on the presence of the Enp2-Bfr2-Lcp5 core, which upon binding to the Kre33 dimer completes 90S assembly (see Discussion).

To consider a distinct Kre33 mutant rather a degron allele, we investigated a previously isolated yeast *kre33-1* temperature-sensitive (*ts*) mutant (Figure 6A) obtained in a genetic screen for 40S subunit export mutants (Grandi et al., 2002). To understand the molecular basis for its *ts* phenotype in the context of the thermophile 90S cryo-EM structure, we cloned the *kre33-1* gene locus including a 5' promoter and a 3' non-coding region and sequenced it. This revealed a single point mutation in the *KRE33* ORF, changing the highly conserved L789 residue into a phenylalanine (Figure 6B). When this *kre33-1* (L789F) allele was inserted into a single-copy plasmid and transformed into the otherwise lethal *kre33Δ* null strain, the original *ts* phenotype of *kre33-1* and a decrease of 40S subunits in polysome gradients could be re-established (Figure 6A and Figure S4A) (see also (Grandi et al., 2002). Whole cell lysate western blots indicated that the mutant Kre33 L789F protein was produced at 23°C, but levels were somewhat reduced after shifting to the restrictive temperature (Figure S4B and S4C). These data suggest that the L789F mutation affects expression and association of Kre33 with 90S pre-ribosomes.

Next, we aimed to determine the position of the homologous *ctKre33* residue L790 that corresponds to the critical *scKre33* L789 (Figure 6B) in our improved cryo-EM map. Herein, almost the entire *ctKre33* homodimer was resolved to near atomic resolution (Figures 2B and 6C), which revealed that the highly conserved *ctKre33* L790 is surrounded by several other conserved hydrophobic residues (*ctKre33* F786, L787, L789, F794, F797, L885, and L889) (Figure 6C). In a wider structural context, *ctKre33* L790 is part of a conserved C-terminal domain, which is intimately connected with a GCN5-related N-acetyltransferase (GNAT) domain that itself is fused to an RNA helicase domain

(Chimnaronk et al., 2009). As seen in the cryo-EM map, the Kre33 C-domain dimerizes with the equivalent C-domain of the second Kre33 copy on the 90S pre-ribosomal surface (Figure 2B). Thus, it is conceivable that the mutated F789 residue, which is bulkier than the original L789, does not optimally fit into this hydrophobic interaction network, thereby affecting the overall Kre33 C-domain topology and consequently impairing Kre33 dimerization. Consistent with this interpretation, scKre33 L789F was less associated with pre-ribosomes on sucrose gradients and was less dimerized on the affinity-purified 90S particle (Figure S4A and S4D; data not shown).

Based on the *Chaetomium thermophilum* cryo-EM map, we designed a second-site suppressor mutation in *kre33-1*, by mutating scKre33 F785 (corresponding to ctKre33 F786), a nearby residue also protruding into the same hydrophobic pocket as L789, to a less bulky leucine. As anticipated, growth of the scKre33 L789F–F785L double mutant was significantly improved at the restrictive temperature (Figure 6A), which is satisfying evidence of the quality of our 90S cryo-EM map. Notably, scKre33 L789 is extremely conserved and found in almost all Kre33-expressing species up to human (Figure 6B). However, a few species such as *Sarcoptes scabiei* (S.s., parasitic arthropod mite) have evolutionarily changed the analogous scKre33 L789 to a phenylalanine, but at the same time F786 has reverted to a leucine (Figure 6B), which together might be compensatory mutations supporting our experimental suppression data.

Motivated by these findings, we screened for random suppressor mutants in the *kre33-1* strain. Several spontaneous suppressors arose, which all were dependent on the plasmid-linked *kre33-1* ORF. Sequencing of the best suppressor allele revealed back mutation to the original L789 (*KRE33*: CTT Leu; *kre33-1*: TTT Phe; *kre33-1* suppressor #1: TTG Leu). The other suppressors, which did not reach optimal growth at 37 °C, exhibited second-site mutations such as L864H, L864R, or R748S in the *kre33-1* allele (Figure 6A and 6B). Significantly, residue L864 forms a contact with L786 that is also part of the hydrophobic network into which L789 is integrated (Figure 6C). Thus, we interpret this second-site L864H or R suppression as directly influencing this hydrophobic network, which might ultimately affect the folding and/or topology of the entire Kre33 C-domain (see Discussion).

Structure-Based Mutations in the Bfr2 C-terminus Impair Kre33 Module Assembly

To extend the structure-based mutational analysis of the Kre33 module, we generated mutants in Bfr2. Specifically, Bfr2 was progressively truncated from the C-terminus (Figure 7A and S5C), which has direct contact to Enp2 by meandering over the Enp2 β -propeller surface (see also Figure 2B). Importantly, via a short α -helical segment in this C-terminal sequence (residues 569–574; called wedge helix), Bfr2 also makes contact to the Kre33 proximal subunit (Figure 7A). *In vivo*, the highly conserved Bfr2 C-terminus is essential for cell growth (Bfr2 Δ C3; deletion of residues 432–534 in yeast). However, removal of the wedge helix (Bfr2 Δ C2, residues 488–534 in yeast) yielded cells with a cold-sensitive growth defect (Figure 7B, left panel; Figure S5A). Affinity purification of Bfr2's partner protein Enp2 from *bfr2* Δ C2 cells showed that Enp2 still interacted with Kre33 and both were present on 90S particles, but Bfr2 Δ C2 and Lcp5 were markedly absent (Figure 7B, middle panel). Consistent with this finding, affinity-purified Bfr2 Δ C2-FTpA was still associated with Lcp5, but Enp2 and Kre33 were significantly absent (Figure 7B, right panel). Altogether, this data point to a key role of the Bfr2 C-terminal wedge helix in tethering the Bfr2-Lcp5 heterodimer to the Enp2 β -propeller-Kre33 (distal) assemblage, which drives 90S maturation (see Discussion).

Structure-based mutation in the Krr1 C-terminal Helix Reveals a Functional Link to the Enp2 C-terminus of the Kre33 Module

In several of our 90S cryo-EM structures (states B1, B2, C), we noticed a clear α -helical element, which emerges from the central part of the 90S and contacts, with its tip, the Kre33 module at a site where the Bfr2 C-terminus and Enp2 form a composite binding surface (Figure 7A). This α -helix was identified as part of the C-terminal extension of Krr1, which is another 90S factor that is integrated via its two KH domains in the middle part of the 90S structure (Sturm et al., 2017). To clarify the role of this connective α -helix bridging the 5' domain and central platform, we deleted it in yeast, but did not observe a clear-cut growth defect (Figure 7C, left panel; *krr1* Δ C, residues 274–316). However, since this Krr1 α -helix is conserved in evolution, we tested whether the *krr1* Δ C mutation is

essential in the context of other viable mutations, mapping in Kre33 module members but not disturbing module assembly.

For this purpose, we considered the long Enp2 C-terminal extension, which is only partially visible in our 90S structure and apparently is not necessary for the Kre33 module assembly (Figure 7A). Since the second half of the Enp2 C-terminal extension is less conserved than the first (Figure S5B), we deleted it from the yeast Enp2. The derived yeast strain *enp2Δ515–707* (termed *enp2ΔC*) was viable but exhibited a slow growth phenotype at lower temperatures (23°C, Figure 7C, left panel; Figure S5A). As anticipated, this strong growth defect is not due to an impaired formation of the Kre33 module, since affinity-purification of Enp2ΔC-FtpA from yeast cells showed that it was still part of the Kre33-Enp2ΔC-Bfr2-Lcp1 complex, which itself was further assembled into the 90S particle (Figure 7C, middle panel).

Notably, when the *krr1ΔC* allele was combined with the viable mutant lacking the Enp2 C-terminal extension (*enp2ΔC*), we observed a strong, synergistically enhanced phenotype at 30 °C (Figure 7C, left panel), which was further increased upon shifting to 23 °C (Figure S5A, left and right panel). In contrast, such a synergistic genetic relationship was less notable between *enp2ΔC* and *bfr2ΔC2*, or between *enp2ΔC* and *kre33-1* (Figure S5A), pointing to an epistatic relationship. Strikingly, when UTP-A was isolated from the *krr1ΔC enp2ΔC* double mutant, it was predominantly found in its free form and not incorporated into the 90S particles in comparison to the single mutants (Figure 7C, right panel). When other 90S modules (e.g. Pwp2-FTpA for the UTP-B module, or Utp22-FTpA for the UTP-C module) were affinity-purified, they also showed an altered pattern, but this was less prominent than in the case of UTP-A (data not shown). Thus, we conclude from these data that the Krr1 C-helix, although not essential, has an important function for 90S pre-ribosome biogenesis, perhaps by crosslinking and stabilizing major subdomains within the 90S scaffold, or by sensing the correct 5' domain incorporation in the 90S particle (see Discussion).

DISCUSSION

This study reports novel thermophile 90S structures, which shine light on the temporal order of stable 18S rRNA subdomain incorporation, which is mediated by the Kre33 module, and establish the final monolithic 90S pre-ribosome previously defined by cryo-EM. Based on these new structural, biochemical and genetic data, we propose a model for how the asymmetric Kre33 module performs this integrative construction.

An unexpected finding from our study is that the four major 18S rRNA subdomains are not strictly co-transcriptionally (5'>3') incorporated into the 90S particle, which is in contrast to our current thinking. A distinct temporal 90S assembly pathway has been suggested from large sets of structural, biochemical, and yeast genetics data, and in particular from recent *in vivo* assays, in which expressed aptamer-tagged pre-rRNA fragments of variable length were analyzed for the timely recruitment of 90S factors ([Chaker-Margot et al., 2015](#); [Zhang et al., 2016b](#)). Consequently, the stage-specific order of how these 90S factors associate co-transcriptionally along the evolving pre-ribosomal RNA from 5' to 3' was taken as the basis to propose a temporal order of SSU processome/90S assembly. However, this mutational approach might not always faithfully reproduce the physiological assembly pathway, because the generated intermediates with truncated rRNA are dead-end products. As a result, these intermediates can never be involved in a final situation in the presence of the entire 18S rRNA, which could change the direction of the order of assembly. Therefore, it appears useful to distinguish (i) the primary recruitment of factors to the nascent transcript and (ii) structural incorporation into the evolving particle, as separate processes in the assembly pathway.

In contrast to our previous view, that domain incorporation follows the temporal order of transcription, our data suggest that parts of the 3' domain, with the attached Noc4 module, assemble first into the pre-formed 5'-ETS structure (corresponding to the "base"), before the central and 5' domains are incorporated. Notably, the prior incorporation of the 3'-domain-dependent Bms1-Rcl1 heterodimer appears to be crucial for the later stable attachment of the 5' domain. We observe that 90S particles in state A retain a highly flexible 5'

domain with only the small helices h16–h18 already rigidly bound. In this stage, the Enp2–Bfr2–Lcp5 core trimer is likely to be already attached to the 5' domain (see later). However, the vast majority of the 5' domain cannot be resolved at this level by cryo-EM, but becomes visible in the assembly steps that follow its stable incorporation. This step is accompanied by the appearance of the Kre33–Enp2–Bfr2–Lcp5 module, the huge α -solenoid Utp20, and the typical ribosomal S-proteins of the 5' domain. During subsequent steps, Utp30 is exchanged for eS19, and recruitment of eS27 occurs. All these findings suggest that the Kre33–Enp2–Bfr2–Lcp5 module plays a key role in stabilizing this first 90S assembly intermediate by keeping the 5' domain in place. For this integrative function, members of the Kre33 module are located at strategic position. For example, the C-terminal domain of Lcp5 connects from the 5' domain to the body of the nascent 90S particle, or the distal Kre33 copy is docked to the Bms1 GTPase. In addition, this assembly intermediate seems to be also stabilized by Utp20, which wraps around the entire 5' domain. Finally, a C-terminal helix, derived from the Krr1 KH domain and protruding from the platform, contacts the Enp2–Bfr2 seed in the 5' area, which might be a crucial sensor and/or stabilizer of the correct integration of the 5' domain into the 90S particle.

Our new structures do not reveal the exact mechanism of how the Kre33–Enp2–Bfr2–Lcp5 module drives stable 5' domain incorporation, but we can speculate. In the temporally ordered 90S particles, we see in state A that the proximal Kre33 is already attached to the Bms1 complex, and that the distal Kre33 has already dimerized with proximal Kre33. However, the distal Kre33 still appears more flexible, because the entire Kre33 dimer lacks stabilization at the other end by Enp2–Bfr2. We interpret this arrangement such that the Enp2–Bfr2–Lcp5 core complex is first bound to the flexible 18S rRNA 5' domain. In a next step, the whole 5' domain could be stably integrated into the 90S particle by tethering the Enp2–Bfr2–Lcp5 to the Kre33 dimer, which consequently would also stably bring the 5' domain into the 90S particle. The early 5' domain maturation requires a specific set of snoRNAs, including U14 and snR30, as well as a number of 5' domain maturation factors, like the helicases Rok1 and Dbp4, which cooperate with these snoRNAs. Thus, keeping the 5' domain not incorporated into the compact 90S scaffold could provide extra time for the completion of the

5' domain maturation ([Kos and Tollervey, 2005](#); [Martin et al., 2014](#); [Soltanieh et al., 2015](#); [Zhang et al., 2016b](#)).

Consistent with this model, depletion or mutation of Kre33–Enp2–Bfr2–Lcp5 module members does not broadly affect the recruitment of the other 90S factors, but indeed could impair 5' domain integration into the 90S particle. Interestingly, depletion of Enp2 or Bfr2 strongly impaired assembly of Enp2, Bfr2, and Lcp5 into the 90S, but Kre33 recruitment was only moderately affected. This observation is consistent with our other finding that Enp2, Bfr2, and Lcp5 are recruited in a Kre33-independent manner. Moreover, the data regarding the deletion of the Bfr2 C-terminal wedge helix further support our recruitment model. When the Bfr2 wedge helix was removed, attachment of the Bfr2 Δ C-Lcp5 to the meanwhile formed Enp2-Kre33 assemblage was impaired. Along this line, the analysis of truncated 18S rRNA precursors and their recovered 90S factors showed that Enp2, Bfr2, and Lcp5 were already recruited to the pre-rRNA fragment composed only of 5'-ETS and the 18S rRNA 5' domain ([Zhang et al., 2016b](#)).

In this context it is interesting that Kre33 exhibits acetyltransferase activity, which might depend on the ATPase activity integrate in its N-terminal domain ([Chimnaronk et al., 2009](#)). This makes Kre33 a potential key regulator of the described integrative steps in 90S biogenesis, which, when coupled with base acetylation at conserved 18S rRNA sites, might act as a checkpoint for the completion of distinct 90S assembly steps ([Sharma et al., 2015](#)).

Taken together, it is remarkable to find that the stable assembly of the later produced 18S rRNA 3' domain into the 90S occurs earlier than the prior made 5' domain. These proceedings are remarkably similar to what has been recently observed in the earliest pre-60S assembly pathway ([Kater et al., 2017](#); [Sanghai et al., 2018](#); [Zhou et al., 2018](#)). To generalize on these common principles, cells apparently avoid the unwanted assembly of 3' truncated pre-rRNA into pre-ribosomes, which might be generated by premature transcription termination, as it has been observed for Pol II transcription, or by rRNA degradation before assembly is complete. Thus, this would be an elegant way of preventing formation of nonfunctional ribosomal subunits, which otherwise might undergo further unproductive maturation.

Early recruitment of Kre33 by the 3' domains would also allow for timely acetylation of its two cognate sites, one in the 3' major domain and one in the 3' minor domain steps (Sharma et al., 2015) before these domains are buried inside the 90S particle or positioned at an unreachable distance. It is tempting to speculate that the dimer formation of Kre33 allows for one subunit to remain active as an acetyltransferase able to span the distance to its substrate, whereas the second functions by recruiting and anchoring the dimer in the evolving 90S particle. This would be reminiscent of other modifying AF enzymes such as Emg1 or Nop1, which appear as dimers or as two separate copies in the 90S particle, albeit with one or even both subunits having lost their modifying catalytic function in this context.

SUPPLEMENTAL INFORMATION

Supplemental Information includes seven figures and one table and can be found with this article online at <https://doi>.

ACKNOWLEDGEMENTS

E.H. was supported by grants from the DFG (HU363/12-1) and ERC (ADG 741781 GLOWSOME). R.B. acknowledges support by the DFG (BE 1814/15-1) and the European Research Council (Advanced Grants CRYOTRANSLATION).

AUTHOR CONTRIBUTIONS

J.C., J.B., N.K., P.F., B.L., R.B. and E.H. designed the study. N.K. and S.G. established the split-tag affinity-purification method in *Chaetomium thermophilum*. S.G. prepared and characterized the *ctKre33-ctNoc4* sample for cryo-EM and O.B. performed the cryo-EM data collection. J.C. processed the cryo-EM data, built and refined the models. J.C. and R.B. analyzed and interpreted the structures. J.B., R. K. and M.K. performed the work on the yeast and *ctKre33* modules, where D.S. initially isolated the *kre33-1* mutant. B.L. performed the work on the *ctNoc4* module. P.F. performed the genetic and biochemical analysis of the yeast *enp2*, *bfr2* and *krr1* mutants. J.C., J.B., N.K., R.B., and E.H. wrote the manuscript, and all authors commented on the manuscript.

DECLARATION OF INTERESTS

The authors declare no competing interests.

REFERENCES

- Adams, P.D., Afonine, P.V., Bunkoczi, G., Chen, V.B., Davis, I.W., Echols, N., Headd, J.J., Hung, L.W., Kapral, G.J., Grosse-Kunstleve, R.W., *et al.* (2010). PHENIX: a comprehensive Python-based system for macromolecular structure solution. *Acta crystallographica. Section D, Biological crystallography* **66**, 213-221.
- Albert, B., Knight, B., Merwin, J., Martin, V., Ottoz, D., Gloor, Y., Bruzzone, M.J., Rudner, A., and Shore, D. (2016). A Molecular Titration System Coordinates Ribosomal Protein Gene Transcription with Ribosomal RNA Synthesis. *Mol Cell* **64**, 720-733.
- Bammert, L., Jonas, S., Ungricht, R., and Kutay, U. (2016). Human AATF/Che-1 forms a nucleolar protein complex with NGDN and NOL10 required for 40S ribosomal subunit synthesis. *Nucleic Acids Res* **44**, 9803-9820.
- Barandun, J., Chaker-Margot, M., Hunziker, M., Molloy, K.R., Chait, B.T., and Klinge, S. (2017). The complete structure of the small-subunit processome. *Nat Struct Mol Biol* **24**, 944-953.
- Barandun, J., Hunziker, M., and Klinge, S. (2018). Assembly and structure of the SSU processome—a nucleolar precursor of the small ribosomal subunit. *Curr Opin Struct Biol* **49**, 85-93.
- Barrio-Garcia, C., Thoms, M., Flemming, D., Kater, L., Berninghausen, O., Bassler, J., Beckmann, R., and Hurt, E. (2016). Architecture of the Rix1-Rea1 checkpoint machinery during pre-60S-ribosome remodeling. *Nat Struct Mol Biol* **23**, 37-44.
- Bassler, J., Ahmed, Y.L., Kallas, M., Kornprobst, M., Calvino, F.R., Gnadig, M., Thoms, M., Stier, G., Ismail, S., Kharde, S., *et al.* (2017). Interaction network of the ribosome assembly machinery from a eukaryotic thermophile. *Protein Sci* **26**, 327-342.
- Bassler, J., and Hurt, E. (2018). Eukaryotic Ribosome Assembly. *Annu Rev Biochem*.
- Biasini, M., Bienert, S., Waterhouse, A., Arnold, K., Studer, G., Schmidt, T., Kiefer, F., Gallo Cassarino, T., Bertoni, M., Bordoli, L., *et al.* (2014). SWISS-MODEL: modelling protein tertiary and quaternary structure using evolutionary information. *Nucleic Acids Res* **42**, W252-258.
- Buchan, D.W., Minneci, F., Nugent, T.C., Bryson, K., and Jones, D.T. (2013). Scalable web services for the PSIPRED Protein Analysis Workbench. *Nucleic Acids Res* **41**, W349-357.
- Cannio, R., Contursi, P., Rossi, M., and Bartolucci, S. (2001). Thermoadaptation of a mesophilic hygromycin B phosphotransferase by directed evolution in hyperthermophilic Archaea: selection of a stable genetic marker for DNA transfer into *Sulfolobus solfataricus*. *Extremophiles* **5**, 153-159.
- Chaker-Margot, M., Barandun, J., Hunziker, M., and Klinge, S. (2017). Architecture of the yeast small subunit processome. *Science* **355**.

Chaker-Margot, M., Hunziker, M., Barandun, J., Dill, B.D., and Klinge, S. (2015). Stage-specific assembly events of the 6-MDa small-subunit processome initiate eukaryotic ribosome biogenesis. *Nat Struct Mol Biol* 22, 920-923.

Chen, V.B., Arendall, W.B., 3rd, Headd, J.J., Keedy, D.A., Immormino, R.M., Kapral, G.J., Murray, L.W., Richardson, J.S., and Richardson, D.C. (2010). MolProbity: all-atom structure validation for macromolecular crystallography. *Acta crystallographica. Section D, Biological crystallography* 66, 12-21.

Cheng, J., Kellner, N., Berninghausen, O., Hurt, E., and Beckmann, R. (2017). 3.2-A-resolution structure of the 90S preribosome before A1 pre-rRNA cleavage. *Nat Struct Mol Biol* 24, 954-964.

Chimnaronk, S., Suzuki, T., Manita, T., Ikeuchi, Y., Yao, M., Suzuki, T., and Tanaka, I. (2009). RNA helicase module in an acetyltransferase that modifies a specific tRNA anticodon. *EMBO J* 28, 1362-1373.

Delprato, A., Al Kadri, Y., Perebaskine, N., Monfoulet, C., Henry, Y., Henras, A.K., and Fribourg, S. (2014). Crucial role of the Rcl1p-Bms1p interaction for yeast pre-ribosomal RNA processing. *Nucleic Acids Res* 42, 10161-10172.

Emsley, P., and Cowtan, K. (2004). Coot: model-building tools for molecular graphics. *Acta crystallographica. Section D, Biological crystallography* 60, 2126-2132.

Gallagher, J.E., Dunbar, D.A., Granneman, S., Mitchell, B.M., Osheim, Y., Beyer, A.L., and Baserga, S.J. (2004). RNA polymerase I transcription and pre-rRNA processing are linked by specific SSU processome components. *Genes Dev* 18, 2506-2517.

Goddard, T.D., Huang, C.C., Meng, E.C., Pettersen, E.F., Couch, G.S., Morris, J.H., and Ferrin, T.E. (2018). UCSF ChimeraX: Meeting modern challenges in visualization and analysis. *Protein Sci* 27, 14-25.

Grandi, P., Rybin, V., Bassler, J., Petfalski, E., Strauss, D., Marzioch, M., Schäfer, T., Kuster, B., Tschochner, H., Tollervey, D., *et al.* (2002). 90S pre-ribosomes include the 35S pre-rRNA, the U3 snoRNP, and 40S subunit processing factors but predominantly lack 60S synthesis factors. *Mol. Cell* 10, 105-115.

Granneman, S., Gallagher, J.E., Vogelzangs, J., Horstman, W., van Venrooij, W.J., Baserga, S.J., and Pruijn, G.J. (2003). The human Imp3 and Imp4 proteins form a ternary complex with hMpp10, which only interacts with the U3 snoRNA in 60-80S ribonucleoprotein complexes. *Nucleic acids research* 31, 1877-1887.

Hunziker, M., Barandun, J., Petfalski, E., Tan, D., Delan-Forino, C., Molloy, K.R., Kim, K.H., Dunn-Davies, H., Shi, Y., Chaker-Margot, M., *et al.* (2016). UtpA and UtpB chaperone nascent pre-ribosomal RNA and U3 snoRNA to initiate eukaryotic ribosome assembly. *Nature communications* 7, 12090.

Janke, C., Magiera, M.M., Rathfelder, N., Taxis, C., Reber, S., Maekawa, H., Moreno-Borchart, A., Doenges, G., Schwob, E., Schiebel, E., *et al.* (2004). A versatile toolbox for PCR-based tagging of yeast genes: new fluorescent proteins, more markers and promoter substitution cassettes. *Yeast* 21, 947-962.

Kater, L., Thoms, M., Barrio-Garcia, C., Cheng, J., Ismail, S., Ahmed, Y.L., Bange, G., Kressler, D., Berninghausen, O., Sinning, I., *et al.* (2017). Visualizing the Assembly Pathway of Nucleolar Pre-60S Ribosomes. *Cell* 171, 1599-1610 e1514.

Kellner, N., Schwarz, J., Sturm, M., Fernandez-Martinez, J., Griesel, S., Zhang, W., Chait, B.T., Rout, M.P., Kuck, U., and Hurt, E. (2016). Developing genetic

tools to exploit *Chaetomium thermophilum* for biochemical analyses of eukaryotic macromolecular assemblies. *Sci Rep* 6, 20937.

Kimanius, D., Forsberg, B.O., Scheres, S.H., and Lindahl, E. (2016). Accelerated cryo-EM structure determination with parallelisation using GPUs in RELION-2. *eLife* 5.

Klinge, S., and Woolford, J.L., Jr. (2018). Ribosome assembly coming into focus. *Nat Rev Mol Cell Biol*.

Kornprobst, M., Turk, M., Kellner, N., Cheng, J., Flemming, D., Kos-Braun, I., Kos, M., Thoms, M., Berninghausen, O., Beckmann, R., *et al.* (2016). Architecture of the 90S Pre-ribosome: A Structural View on the Birth of the Eukaryotic Ribosome. *Cell* 166, 380-393.

Kos, M., and Tollervey, D. (2005). The Putative RNA Helicase Dbp4p Is Required for Release of the U14 snoRNA from Preribosomes in *Saccharomyces cerevisiae*. *Mol Cell* 20, 53-64.

Krogan, N.J., Peng, W.T., Cagney, G., Robinson, M.D., Haw, R., Zhong, G., Guo, X., Zhang, X., Canadian, V., Richards, D.P., *et al.* (2004). High-definition macromolecular composition of yeast RNA-processing complexes. *Mol Cell* 13, 225-239.

Kuhn, H., Hierlmeier, T., Merl, J., Jakob, S., Aguisa-Toure, A.H., Milkereit, P., and Tschochner, H. (2009). The Noc-domain containing C-terminus of Noc4p mediates both formation of the Noc4p-Nop14p submodule and its incorporation into the SSU processome. *PLoS one* 4, e8370.

Lin, J., Lu, J., Feng, Y., Sun, M., and Ye, K. (2013). An RNA-binding complex involved in ribosome biogenesis contains a protein with homology to tRNA CCA-adding enzyme. *PLoS Biol* 11, e1001669.

Liu, P.C., and Thiele, D.J. (2001). Novel stress-responsive genes EMG1 and NOP14 encode conserved, interacting proteins required for 40S ribosome biogenesis. *Mol Biol Cell* 12, 3644-3657.

Longtine, M.S., McKenzie, A., Demarini, D.J., Shah, N.G., Wach, A., Brachat, A., Philippsen, P., and Pringle, J.R. (1998). Additional modules for versatile and economical PCR-based gene deletion and modification in *Saccharomyces cerevisiae*. *Yeast* 10, 953-961.

Martin, R., Hackert, P., Ruprecht, M., Simm, S., Bruning, L., Mirus, O., Sloan, K.E., Kudla, G., Schleiff, E., and Bohnsack, M.T. (2014). A pre-ribosomal RNA interaction network involving snoRNAs and the Rok1 helicase. *RNA* 20, 1173-1182.

Matsuo, Y., Granneman, S., Thoms, M., Manikas, R.G., Tollervey, D., and Hurt, E. (2014). Coupled GTPase and remodelling ATPase activities form a checkpoint for ribosome export. *Nature* 505, 112-116.

Perez-Fernandez, J., Martin-Marcos, P., and Dosil, M. (2011). Elucidation of the assembly events required for the recruitment of Utp20, Imp4 and Bms1 onto nascent pre-ribosomes. *Nucleic Acids Res* 39, 8105-8121.

Perez-Fernandez, J., Roman, A., De Las Rivas, J., Bustelo, X.R., and Dosil, M. (2007). The 90S preribosome is a multimodular structure that is assembled through a hierarchical mechanism. *Mol Cell Biol* 27, 5414-5429.

Pettersen, E.F., Goddard, T.D., Huang, C.C., Couch, G.S., Greenblatt, D.M., Meng, E.C., and Ferrin, T.E. (2004). UCSF Chimera--a visualization system for exploratory research and analysis. *J Comput Chem* 25, 1605-1612.

Pöll, G., Li, S., Ohmayer, U., Hierlmeier, T., Milkereit, P., and Perez-Fernandez, J. (2014). In vitro reconstitution of yeast tUTP/UTP A and UTP B subcomplexes provides new insights into their modular architecture. *PLoS one* 9, e114898.

Rohou, A., and Grigorieff, N. (2015). CTFFIND4: Fast and accurate defocus estimation from electron micrographs. *J Struct Biol* 192, 216-221.

Sa-Moura, B., Kornprobst, M., Kharde, S., Ahmed, Y.L., Stier, G., Kunze, R., Sinning, I., and Hurt, E. (2017). Mpp10 represents a platform for the interaction of multiple factors within the 90S pre-ribosome. *PLoS one* 12, e0183272.

Sanghai, Z.A., Miller, L., Molloy, K.R., Barandun, J., Hunziker, M., Chaker-Margot, M., Wang, J., Chait, B.T., and Klinge, S. (2018). Modular assembly of the nucleolar pre-60S ribosomal subunit. *Nature* 556, 126-129.

Sharma, S., Langhendries, J.L., Watzinger, P., Kotter, P., Entian, K.D., and Lafontaine, D.L. (2015). Yeast Kre33 and human NAT10 are conserved 18S rRNA cytosine acetyltransferases that modify tRNAs assisted by the adaptor Tan1/THUMP1. *Nucleic Acids Res* 43, 2242-2258.

Soltanieh, S., Lapensee, M., and Dragon, F. (2014). Nucleolar proteins Bfr2 and Enp2 interact with DEAD-box RNA helicase Dbp4 in two different complexes. *Nucleic Acids Res* 42, 3194-3206.

Soltanieh, S., Osheim, Y.N., Spasov, K., Trahan, C., Beyer, A.L., and Dragon, F. (2015). DEAD-box RNA helicase Dbp4 is required for small-subunit processome formation and function. *Mol Cell Biol* 35, 816-830.

Sun, Q., Zhu, X., Qi, J., An, W., Lan, P., Tan, D., Chen, R., Wang, B., Zheng, S., Zhang, C., *et al.* (2017). Molecular architecture of the 90S small subunit pre-ribosome. *eLife* 6.

Wegierski, T., Billy, E., Nasr, F., and Filipowicz, W. (2001). Bms1p, a G-domain-containing protein, associates with Rcl1p and is required for 18S rRNA biogenesis in yeast. *RNA* 7, 1254-1267.

Zhang, C., Sun, Q., Chen, R., Chen, X., Lin, J., and Ye, K. (2016a). Integrative structural analysis of the UTPB complex, an early assembly factor for eukaryotic small ribosomal subunits. *Nucleic Acids Res* 44, 7475-7486.

Zhang, K. (2016). Gctf: Real-time CTF determination and correction. *J Struct Biol* 193, 1-12.

Zhang, K. (2017). Gautomatch. <http://www.mrc-lmb.cam.ac.uk/kzhang/Gautomatch/>.

Zhang, L., Wu, C., Cai, G., Chen, S., and Ye, K. (2016b). Stepwise and dynamic assembly of the earliest precursors of small ribosomal subunits in yeast. *Genes Dev* 30, 718-732.

Zheng, S.Q., Palovcak, E., Armache, J.P., Verba, K.A., Cheng, Y., and Agard, D.A. (2017). MotionCor2: anisotropic correction of beam-induced motion for improved cryo-electron microscopy. *Nat Methods* 14, 331-332.

Zhou, D., Zhu, X., Zheng, S., Tan, D., Dong, M.Q., and Ye, K. (2018). Cryo-EM structure of an early precursor of large ribosomal subunit reveals a half-assembled intermediate. *Protein Cell*.

STAR ★ Methods

Plasmid Table

Plasmid Name	Genotype	Ref
YCplac111-TAP-Flag-scUtp18	TAP-Flag- <i>UTP18</i> , <i>LEU2</i> , ARS/ CEN	
pNK124	<i>pERG1_P_{NOC4}-NOC4-Flag-T_{gpd}</i>	
pNK130	<i>pHPH_P_{KRE33}:KRE33-TEV-ProtA:T_{gpd}</i>	
pRS416 Bfr2	<i>P_{BFR2}-BFR2GS-T_{ADH1}</i> , <i>URA3</i> , ARS/CEN, AmpR	
pRS416 Enp2	<i>P_{ENP2}-ENP2GS-T_{ADH1}</i> , <i>URA3</i> , ARS/CEN	
pRS416 Kre33	<i>P_{KRE33}-KRE33GS-T_{ADH1}</i> , <i>URA3</i> , ARS/CEN	
pRS315 KRE33 FTpA	<i>KRE33-Flag-TEV-protA</i> , <i>LEU2</i> , ARS/Cen	
pRS315 <i>kre33-1</i> FTpA	<i>P_{KRE33}-kre33-1-Flag-TEV-protA-T_{ADH1}</i> , <i>LEU2</i> , ARS/Cen, <i>kre33 L789F</i>	
pRS314 <i>kre33</i> F785L, L789F FTpA	<i>P_{KRE33}-kre33-1-Flag-TEV-protA-T_{ADH1}</i> , <i>LEU2</i> , ARS/Cen, <i>kre33 F785L, L789F</i>	
pRS315 KRE33 reverted FTpA	<i>P_{KRE33}-kre33-1-Flag-TEV-protA-T_{ADH1}</i> , <i>LEU2</i> , ARS/Cen,	
pRS315 <i>kre33</i> L789F, L864R FTpA	<i>P_{KRE33}-kre33-1-Flag-TEV-protA-T_{ADH1}</i> , <i>LEU2</i> , ARS/Cen, L789F, L864R	
pRS315 <i>kre33</i> L789F, L864H FTpA	<i>P_{KRE33}-kre33-1-Flag-TEV-protA-T_{ADH1}</i> , <i>LEU2</i> , ARS/Cen, L789F, L864H	
pRS315 <i>kre33</i> L789F, R748S FTpA	<i>P_{KRE33}-kre33-1-Flag-TEV-protA-T_{ADH1}</i> , <i>LEU2</i> , ARS/Cen, L789F, R748S	
pMT_LEU2 ptA-TEV ctBFR2 Pgal ctKre33	<i>P_{GAL1-10}-ptA-TEV-ctBFR2-T_{ADH1}</i> , <i>P_{GAL1-10} ctKre33</i> , 2 μ , <i>LEU2</i>	
pMT_URA3 HA-ctLcp5 Pgal	<i>P_{GAL1-10}-HA-ctLCP5-T_{ADH1}</i> , 2 μ , <i>URA3</i>	
pMT_TRP1 ctENP2-Flag2 Pgal	<i>P_{GAL1-10} -ctENP2-2xFlag-T_{ADH1}</i> , 2 μ , <i>TRP1</i>	
pMT_LEU2 ptA-TEV ctKre33 Pgal	<i>P_{GAL1-10}-ptA-TEV-ctKRE33-T_{ADH1}</i> , 2 μ , <i>LEU2</i>	
pMT_LEU2 ptA-TEV ctBfr2	<i>P_{GAL1-10} -ptA-TEV-ctBFR2-T_{ADH1}</i> , 2 μ , <i>LEU2</i>	
pMT_TRP1 Flag-ctKre33 Pgal	<i>P_{GAL1-10} -3xFlag-ctKRE33-T_{ADH1}</i> , 2 μ , <i>TRP1</i>	
pMT_TRP1 Flag-ctLcp5 Pgal	<i>P_{GAL1-10} -3xFlag-ctLCP5-T_{ADH1}</i> , 2 μ , <i>TRP1</i>	
pRS314 yEnp2-eGFP	<i>P_{ENP2}-ENP2-GFP-T_{ADH1}</i> , ARS/CEN, <i>TRP1</i>	

pRS314 yBfr2-eGFP	P_{BFR2} - <i>BFR2</i> -GFP- T_{ADH1} ARS/CEN, <i>TRP1</i>	
YCplac111 Prsa4 GFP-yLCP5	P_{RSA4} -GFP-LCP5- T_{ADH1} ARS/CEN, <i>LEU2</i>	
pRS314 yKre33 GFP	P_{KRE33} - <i>KRE33</i> -GFP- T_{ADH1} , ARS/CEN, <i>TRP1</i>	
pGADT7 ctBfr2	Gal4 AD- <i>ctBFR2</i> - T_{ADH1} , <i>LEU2</i> , <i>AmpR</i>	1
pG4ADC111 ctEnp2	<i>ctENP2</i> -Gal4 AD- T_{ADH1} , <i>LEU2</i> , <i>AmpR</i>	
pGADT7 ctLcp5	Gal4 AD- <i>ctLCP5</i> - T_{ADH1} , <i>LEU2</i> , <i>AmpR</i>	1
pGADT7 ctKre33	Gal4 AD- <i>ctKRE33</i> - T_{ADH1} , <i>LEU2</i> , <i>AmpR</i>	1
pGBKT7 ctBfr2	Gal4 DNA-BD- <i>ctBFR2</i> - T_{ADH1} , <i>TRP1</i> , <i>KanR</i>	1
pG4BDC22 ctEnp2	<i>ctENP2</i> -Gal4 DNA-BD- T_{ADH1} , <i>TRP1</i> , <i>AmpR</i>	
pGBKT7 ctLcp5	Gal4 DNA-BD- <i>ctLCP5</i> - T_{ADH1} , <i>TRP1</i> , <i>KanR</i>	1
pGBKT7 ctKre33	Gal4 DNA-BD- <i>ctKRE33</i> - T_{ADH1} , <i>TRP1</i> , <i>KanR</i>	1
pRS316 Krr1	P_{KRR1} - <i>KRR1</i> - T_{KRR1} , URA3, ARS/CEN, <i>AmpR</i>	
pRS314 Krr1	P_{KRR1} - <i>KRR1</i> - T_{KRR1} , <i>TRP1</i> , ARS/CEN, <i>AmpR</i>	
pRS314 <i>krr1</i> Δ C	P_{KRR1} - <i>krr1</i> Δ C- T_{KRR1} , <i>TRP1</i> , ARS/CEN, <i>AmpR</i>	
pRS315 Krr1	P_{KRR1} - <i>KRR1</i> - T_{KRR1} , <i>LEU2</i> , ARS/CEN, <i>AmpR</i>	
pRS315 <i>krr1</i> Δ C	P_{KRR1} - <i>krr1</i> Δ C- T_{KRR1} , <i>LEU2</i> , ARS/CEN, <i>AmpR</i>	
pRS315 <i>bfr2</i> Δ C3	P_{BFR2} - <i>bfr2</i> Δ C3- T_{ADH1} , <i>LEU2</i> , ARS/CEN, <i>AmpR</i>	
pRS315 <i>bfr2</i> Δ C2	P_{BFR2} - <i>bfr2</i> Δ C2- T_{ADH1} , <i>LEU2</i> , ARS/CEN, <i>AmpR</i>	
pRS315 <i>bfr2</i> Δ C1	P_{BFR2} - <i>bfr2</i> Δ C1- T_{ADH1} , <i>LEU2</i> , ARS/CEN, <i>AmpR</i>	
pRS314 Enp2	P_{ENP2} - <i>ENP2</i> - T_{ADH1} , <i>TRP1</i> , ARS/CEN, <i>AmpR</i>	
pRS314 <i>enp2</i> Δ C	P_{ENP2} - <i>enp2</i> Δ C- T_{ADH1} , <i>TRP1</i> , ARS/CEN, <i>AmpR</i>	
pRS314 <i>kre33-1</i>	P_{KRE33} - <i>kre33-1</i> - T_{ADH1} , <i>TRP1</i> , ARS/CEN , <i>AmpR</i>	
pRS315 Bfr2	P_{BFR2} - <i>BFR2</i> - T_{ADH1} , <i>LEU2</i> , ARS/CEN, <i>AmpR</i>	
pRS315 Enp2-FTpA	P_{ENP2} - <i>ENP2</i> -Flag-TEV-ProtA- T_{ADH1} , <i>LEU2</i> , ARS/CEN, <i>AmpR</i>	
pRS315 Enp2 Δ C- FTpA	P_{ENP2} - <i>enp2</i> Δ C-Flag-TEV-ProtA- T_{ADH1} , <i>LEU2</i> , ARS/CEN, <i>AmpR</i>	
pRS315 Bfr2-FTpA	P_{BFR2} - <i>BFR2</i> -Flag-TEV-ProtA- T_{ADH1} , <i>LEU2</i> , ARS/CEN, <i>AmpR</i>	
pRS315 Bfr2 Δ C2- FTpA	P_{BFR2} - <i>bfr2</i> Δ C2-Flag-TEV-ProtA- T_{ADH1} , <i>LEU2</i> , ARS/CEN, <i>AmpR</i>	

pRS313 scRrp12	P_{RRP12} - <i>RRP12</i> - T_{RRP12} , <i>HIS3</i> , ARS/CEN, <i>AmpR</i>	
pRS313 scRrp12 (1-1039aa)	P_{RRP12} - <i>rrp12</i> (1-1039aa)- T_{RRP12} , <i>HIS3</i> , ARS/CEN, <i>AmpR</i>	
pG4ADC111 ctRrp12	<i>ctRRP12</i> -Gal4 AD, <i>LEU2</i> , <i>AmpR</i>	
pGADT7 ctEnp1	Gal4 AD- <i>ctENP1</i> , <i>LEU2</i> , <i>AmpR</i>	1
pGADT7 ctNop14	Gal4 AD- <i>ctNOP14</i> , <i>LEU2</i> , <i>AmpR</i>	1
pGADT7 ctNoc4	Gal4 AD- <i>ctNOC4</i> , <i>LEU2</i> , <i>AmpR</i>	1
pGADT7 ctEmg1	Gal4 AD- <i>ctEMG1</i> , <i>LEU2</i> , <i>AmpR</i>	1
pG4BDC22 ctRrp12	<i>ctRRP12</i> -Gal4 DNA-BD, <i>TRP1</i> , <i>AmpR</i>	
pGBKT7 ctEnp1	Gal4 DNA-BD- <i>ctENP1</i> , <i>TRP1</i> , <i>KanR</i>	1
pGBKT7 ctNop14	Gal4 DNA-BD- <i>ctNOP14</i> , <i>TRP1</i> , <i>KanR</i>	1
pGBKT7 ctNoc4	Gal4 DNA-BD- <i>ctNOC4</i> , <i>TRP1</i> , <i>KanR</i>	1
pGBKT7 ctEmg1	Gal4 DNA-BD- <i>ctEMG1</i> , <i>TRP1</i> , <i>KanR</i>	1
pMT_LEU2 ptA-TEV ctEnp1 Pgal	$P_{GAL1-10}$ -ptA-TEV- <i>ctENP1</i> , <i>LEU2</i> , 2μ ,	
pMT_LEU2 ctRrp12 (1-1039aa) TEV-ptA Pgal	$P_{GAL1-10}$ -ctRrp12 (1-1039) TEV-ptA, <i>LEU2</i> , 2μ , <i>AmpR</i>	
pMT_LEU2 ptA-TEV ctNop14 Pgal	$P_{GAL1-10}$ -ptA-TEV- <i>ctNOP14</i> , 2μ , <i>LEU2</i> , 2μ , <i>AmpR</i>	
pMT_TRP1 Flag-ctEnp1 Pgal	$P_{GAL1-10}$ -Flag- <i>ctENP1</i> , <i>TRP1</i> , 2μ , <i>AmpR</i>	
pMT_TRP1 ctRrp12 (1-1039aa)-Flag Pgal	$P_{GAL1-10}$ - <i>ct rrp12</i> (1-1039aa)-Flag, <i>TRP1</i> , 2μ , <i>AmpR</i>	
pMT_TRP1 3Flag-ctEmg1 Pgal	$P_{GAL1-10}$ -3xFlag- <i>ctEMG1</i> , <i>TRP1</i> , 2μ , <i>AmpR</i>	
pMT_TRP1 3Flag-ctNoc4 Pgal	$P_{GAL1-10}$ -3xFlag- <i>ctNOC4</i> , 2μ , <i>TRP1</i> , 2μ , <i>AmpR</i>	
pMT_TRP1 3Flag-ctEmg1 Pgal ctNoc4	$P_{GAL1-10}$ -3xFlag- <i>ctEMG1</i> , Pgal1-10 <i>ctNoc4</i> , <i>TRP1</i> , 2μ , <i>AmpR</i>	
pMT_URA3 HA-ctNoc4 Pgal	$P_{GAL1-10}$ -HA- <i>ctNOC4</i> , <i>URA3</i> , 2μ , <i>AmpR</i>	
pMT_URA3 HA-ctNop14 Pgal	$P_{GAL1-10}$ -HA- <i>ctNOP14</i> , <i>URA3</i> , 2μ , <i>AmpR</i>	

P denotes promoter, T terminator

Reference 1

Bassler, J., Ahmed, Y.L., Kallas, M., Kornprobst, M., Calvino, F.R., Gnadig, M., Thoms, M., Stier, G., Ismail, S., Kharde, S., *et al.* (2017). Interaction network of the ribosome assembly machinery from a eukaryotic thermophile. *Protein Sci* 26, 327-342.

(Bassler et al., 2017)(Bassler et al., 2017)

Saccharomyces cerevisiae strains

Yeast Name	Genotype	Reference
PJ69-4	<i>trp1-901, leu2-3,112,ura3-52, his3-200, gal4Δ, gal80Δ, LYS2::P_{GAL1}-HIS3, P_{GAL2}-ADE2, met2::P_{GAL7}-lacZ</i>	
W303	<i>ade2-1, trp1-1, leu2-3,112, his3-11,15, ura3-1, can1-100</i>	
Utp10-FTpA	<i>UTP10-FTpA::natNT2, W303</i>	
Kre33-FTpA	<i>KRE33-FTpA::HIS3, W303</i>	
Bfr2-FTpA	<i>BFR2-FTpA::HIS3, W303</i>	
Enp2-FTpA	<i>ENP2-FTpA::HIS3, W303</i>	
FTpA-Lcp5	<i>natNT2::P_{LCP5}-ProtA-TEV-Flag-LCP5</i>	
Kre33 shuffle strain	<i>kre33::HIS3, W303 [pRS316 KRE33]</i>	
Enp1-FTpA Bfr2-AID	<i>W303, Padh osTIR1::TRP1, ENP1-FTpA::natNT2, BFR2-HA- AID::HIS3</i>	
Enp1-FTpA Enp2- AID	<i>W303, P_{ADH1} osTIR1::TRP1, ENP1-FTpA::natNT2, ENP2-HA- AID::HIS3</i>	
Enp1-FTpA Kre33-AID	<i>W303, P_{ADH1} osTIR1::TRP1, ENP1-FTpA::natNT2, KRE33-HA- AID::HIS3</i>	
Kre33-Enp2 double shuffle	<i>W303, kre33::HIS3, enp2::natNT2 [pRS316 KRE33, pRS316 ENP2]</i>	
Utp10-FTpA Bfr2- AID	<i>W303, P_{ADH1} osTIR1::TRP1, UTP10-FTpA::natNT2, BFR2-AID -HA::HIS3</i>	
Utp10-FTpA Enp2-AID	<i>W303, P_{ADH1} osTIR1::TRP1, UTP10-FTpA::natNT2, ENP2-AID -HA::HIS3</i>	
Utp10-FTpA Kre33-AID	<i>W303, P_{ADH1} osTIR1::TRP1, UTP10-FTpA::natNT2, KRE33-AID -HA::HIS3</i>	
Bennis Stamm	Bennis Stamm	
Krr1 shuffle	<i>W303, krr1::HIS3 [pRS316 KRR1]</i>	
Krr1 shuffle <i>enp2ΔC</i>	<i>W303, krr1::HIS3, W303, enp2ΔC::hphNT1</i>	
Krr1 shuffle <i>enp2ΔC</i> Utp10-FTpA	<i>W303, krr1::HIS3, W303, enp2ΔC::hphNT1, UTP10-FTpA::natNT2</i>	
Bfr2 shuffle Enp2-FTpA	<i>W303, bfr2::HIS3, ENP2-FTpA::natNT2 [pRS316 BFR2, pRS316 ENP2]</i>	

Krr1-Enp2 double shuffle	W303, <i>krr1</i> ::HIS3, <i>enp2</i> ::hphNT1 [pRS316 <i>KRR1</i> , pRS316 <i>ENP2</i>]	
Krr1-Bfr2 double shuffle	W303, <i>krr1</i> ::HIS3, <i>bfr2</i> ::hphNT1 [pRS316 <i>KRR1</i> , pRS316 <i>BFR2</i>]	
Enp2-Bfr2 double shuffle	W303, <i>enp2</i> ::HIS3, <i>bfr2</i> ::hphNT1 [pRS316 <i>ENP2</i> , pRS316 <i>KRR1</i>]	
Krr1-Kre33 double shuffle	W303, <i>kre33</i> ::HIS3, <i>krr1</i> ::hphNT1 [pRS316 <i>KRE33</i> , pRS316 <i>KRR1</i>]	

***Chaetomium thermophilum* strain**

Name	Genotype
CT48	P_{ACT1} - <i>HPHNT1</i> - T_{GPD} - P_{KRE33} - <i>KRE33</i> -TEV-ProtA- T_{GPD} P_{ACT1} - <i>ERG1</i> - T_{GPD} - P_{NOC4} - <i>NOC4</i> -Flag- T_{GPD}

Cryo-EM data collection, refinement and validation statistics of state B1

	State B1
Data collection and processing	
Magnification	129,151
Voltage (kV)	300
Electron exposure (e-/Å ²)	28
Defocus range (µm)	-1 to -2.5
Pixel size (Å)	1.084
Symmetry imposed	C1
Initial particle images (no.)	1,325,646
Final particle images (no.)	343,726
Map resolution (Å)	3.5
FSC threshold	0.143
Refinement	
Initial model used (PDB code)	5OQL
Model resolution (Å)	3.5
FSC threshold	0.5
Map sharpening B factor (Å ²)	-116
Model composition	
Non-hydrogen atoms	221,434
Protein residues	23,499
RNA	1805
Ligands	3
B factors (Å ²)	
Protein	40.65
RNA	66.02
Ligand	15.71
R.m.s. deviations	
Bond lengths (Å)	0.011
Bond angles (°)	1.29
Validation	
MolProbity score	2.10
Clashscore	6.38
Poor rotamers (%)	2.78
Ramachandran plot	
Favored (%)	93.74
Allowed (%)	6.11
Disallowed (%)	0.15

Isolation of 90S Pre-ribosome Assembly Intermediates from *Chaetomium thermophilum* by Split-Tag Affinity Purification

Growth conditions and media for the cultivation of *Chaetomium thermophilum* strains as well as transformation of *Chaetomium thermophilum* protoplasts followed the protocols described previously (Kellner et al., 2016). In brief, protoplasts were obtained from a submerged culture upon digestion of the mycelium with lysing enzymes from *Trichoderma harzianum* (Sigma–Aldrich cat. no. L1412) for 3–4 h. The resulting protoplasts were filtered, washed and subsequently transformed with 5–10 µg of linearized plasmid DNA. The transformed protoplasts were then directly plated onto two-layered CCM-Sorb agar plates containing the selecting antibiotic in the lower layer, which was overlaid with 10 ml agar without antibiotic to allow recovery of fungal mycelium prior to the action of the selecting agent. Thus, the rate of obtained positive transformants could be greatly increased.

For affinity purification of the *ctKre33* and *ctNoc4* modules, two constructs were created and transformed into the *Chaetomium thermophilum* wildtype strain in two consecutive transformation reactions. First, the *ctKRE33* ORF (CTHT_0016220) including the sequence 1.5 kb upstream of the ORF, comprising the endogenous promoter region, was amplified from genomic DNA and C-terminally fused to the ProtA-TEV-tag and this cassette was coupled to the thermostable *hph* marker. The hygromycin resistance cassette contained a heat-adapted hygromycin phosphotransferase (*hph*) marker from *E. coli* (Cannio et al., 2001) under control of a 750 bp fragment of the constitutively active *actin* promoter (CTHT_0062070) for strong expression levels. For transcription termination a 300 bp fragment downstream of the glyceraldehyde-3-phosphate dehydrogenase (*gapdh*) ORF (CTHT_0004880) was included. Positive integration events were obtained upon transformation subsequent cultivation on hygromycin-supplemented CCM-Sorb medium (200 µg/ml Hygromycin B in bottom layer) at slightly decreased temperatures (42 °C), which was indispensable for retaining functionality of the resistance protein. After verification of the successful integration this strain could be cultivated again at the optimal growth temperature of 50–52°C. For the second construct, the *ctNOC4* ORF (CTHT_0003370) that included a 1.5 kb promoter fragment was C-terminally

fused to the Flag-tag and coupled to the *ERG1* marker conferring terbinafine resistance. This construct was transformed into the *ctKre33-ProtA* strain, followed by selection of terbinafine-resistant colonies (1 µg/ml terbinafine hydrochloride in bottom layer) and expression tests. Co-expression of both tagged fusion proteins was demonstrated by immunoblotting of whole-cell lysates, applying PAP (Sigma–Aldrich cat. no. P1291) and Flag (Sigma–Aldrich cat. no. A8592) antibodies according to the manufacturer’s instructions.

Affinity purification of the resulting *ctKre33-ProtA_ctNoc4-Flag* strain for cryo-EM analysis was performed as described previously (Kellner et al., 2016). The strain was cultivated in 10 l CCM medium and incubated at 50 °C with agitation at 90 rpm for 18 h. After harvesting and washing, the mycelium was dried and ground to a fine powder in a cryogenic cell mill (Retsch MM400). The material was resuspended in NB-Hepes buffer (20 mM Hepes, pH 7.5, 150 mM NaCl, 50 mM KOAc, 2 mM Mg(OAc)₂, 1 mM dithiothreitol, 5% (v/v) glycerol, 0.1% (v/v) IGEPAL CA-630, SIGMAFAST complete protease inhibitor cocktail (Sigma–Aldrich), 3200 U RiboLock RNase inhibitor (Thermo Scientific cat. no. EO0381) and 320 U Qiagen RNase inhibitor (cat. no. 129916)). First, proteins were affinity purified from the cleared supernatant using IgG–Sepharose suspension (IgG–Sepharose 6 Fast Flow, GE Healthcare) and eluted by the TEV protease. In the second affinity purification step the proteins were immobilized on anti-Flag affinity gel (Sigma–Aldrich) and eluted in NB-Hepes buffer containing 2% (v/v) glycerol and 0.003% (v/v) IGEPAL CA-630 by use of 100 µg/ml Flag peptide (Sigma–Aldrich). Eluates were separated by SDS-PAGE and analyzed either by Coomassie staining and mass spectrometry or cryo-EM.

Previously published methods

Yeast two-hybrid analysis of the *Chaetomium thermophilum* factors was performed as previously described (Bassler et al., 2017). The yeast strain PJ69 was transformed with the respective plasmids pGADT7 (N-terminal Gal4 activation domain) and pGBKT7 (N-terminal Gal4 DNA binding domain) and grown on SDC–Trp–Leu–His+2 mM 3-aminotriazole (3AT) or SDC–Trp–Leu–Ade, and analyzed for positive interaction. Note that *ctENP2* and

ctRRP12 were cloned into pG4ADC111 and pG4BDC22 (C-terminal tagging), since N-terminal tagging interferes with their function.

Reconstitution of thermophilic protein complexes was performed as previously described (Bassler et al., 2017). A selective preculture using SDC medium was used to inoculate a YPG culture to induce the expression of *Chaetomium thermophilum* genes under control of the Gal1–10 promoter. After 8 h the cells were harvested and proteins were purified according to standard procedures.

Dimerization of AFs was analyzed according to (Barrio-Garcia et al., 2016). The protein of interest was simultaneously expressed as a Flag-TEV-protein A (FTpA) and GFP-tagged copy and purified via the FTpA tag. Co-purification indicated the presence of multiple copies on the isolated particle/complex.

Depletion of factors using the auxin-inducible degron (aid) system was performed as previously described (Matsuo et al., 2014). The gene of interest was C-terminally modified with the aid tag, which in the presence of auxin is recognized by the *osTIR1* E3 ligase (integrated into the yeast strain), causing ubiquitination and degradation of the protein.

Gene disruption and genomic tagging was performed as described before (Janke et al., 2004; Longtine et al., 1998). All strains were verified by colony PCR, western blot detection of tagged gene variants and phenotype selection. Double shuffle strains were generated via transformation of a phenotype inducing gene variant in the appropriate shuffle strain, selection on FOA to ensure the originally transformed URA3 plasmid was lost, subsequent transformation of a URA3 plasmid containing the second gene, gene disruption and re-introduction of the original URA3 plasmid containing the respective wildtype allele. Phenotype selection at restrictive temperatures (37°C for Kre33 and Krr1 or 23°C for Enp2) ensured that clones transformed with both URA3 plasmids were easily discernable by their bigger colony size.

Electron microscopy and image processing

Purified Kre33–Noc4 sample (3.5 μl) was directly applied onto pre-coated (2 nm) R3/3 holey-carbon-supported copper grids (Quantifoil), blotted for 2–3 s at 4 °C and plunge-frozen in liquid ethane using an FEI Vitrobot Mark IV. Cryo-EM data was acquired on an FEI Titan Krios transmission electron microscope at 300 kV under low-dose conditions (10 frames at about $2.5 \text{ e}^- \text{ \AA}^{-2}$) with a nominal pixel size of 1.084 \AA per pixel on the object scale using the semi-automated software EM-TOOLS (TVIPS). In total, 14,718 micrographs were collected on a Falcon II direct electron detector at nominal defocus ranges from -1.0 to $-2.5 \mu\text{m}$. Original image stacks were aligned, summed and drift-corrected using MotionCor2 (Zheng et al., 2017). Contrast-transfer function (CTF) parameters and resolutions were estimated for each micrograph using CTFIND4 and GCTF, respectively (Rohou and Grigorieff, 2015; Zhang, 2016). Micrographs with an estimated resolution below 5 \AA and an astigmatism below 5% were manually screened for contamination or carbon rupture. A total of 11,465 micrographs were selected and submitted to automated particle picking using Gautomatch with the 90S map as reference (Cheng et al., 2017), resulting in 1,325,646 picked particles (Zhang, 2017). Reference-free 2D classification, 3D refinement and 3D classification (Figure S2) were carried out using Relion V2.1 (Kimanius et al., 2016).

Model building and refinement

In general, the *Chaetomium thermophilum* 90S pre-ribosome structure (PDB ID: 5OQL) was used as an initial model and rigid body fitted in Chimera and Coot (Emsley and Cowtan, 2004; Pettersen et al., 2004). For the molecular modeling of ribosome biogenesis factors that were not, or the majority were not in the reference model (Utp5, Utp8, Utp16, Utp12, Utp13, Utp20, Enp2, Nop14, Noc4, Bfr2, and Lcp5), we initially performed secondary structure prediction (PSIPRED) followed by manual model building in Coot (Buchan et al., 2013; Emsley and Cowtan, 2004). Full molecular models were built for states B1 and B2, whereas working models based on rigid body docking were prepared for all other states, the resolution of which did not allow for *de novo* building.

In states B1 and B2, since only small parts were modelled for Utp4, Utp17, Utp10, and Utp15, we also *de novo* built the missing parts of these factors if density were available. We also built the interface between Kre33 and Bms1, and

the C terminus of Mpp10 and Krr1 proteins. Due to our improved map, we also improved the quality of the models for Kre33, Utp30, Emg1, and Rrp9. In state B2, we still did not have high resolution for Utp-C complex, so a homology model was generated based on the yeast X-ray crystal structure (PDB ID: 4M5D) using the SWISS-MODEL server ([Biasini et al., 2014](#)). The final model was real-space refined with secondary structure restraints using the PHENIX suite ([Adams et al., 2010](#)). Final model evaluation was performed with MolProbity ([Chen et al., 2010](#)).

For states A and a, our model of states B1 or B2 was fitted into the density, before removing or adjusting parts to account for conformational and compositional differences. In general, the 5' domain of the pre-18S rRNA (except h16–18 of pre-18S rRNA), ES6S of pre-18S rRNA, and the associated r-proteins together with Utp20, Enp2, Bfr2, and Lcp5, were omitted from the model.

For state b, our model of state B2 was fitted into the density. The conformational change in the platform region was adjusted manually in Coot and a homology model for Rrp5 was made based on the X-ray crystal structure (PDB ID: 5C9S), which was also the case for state a.

For state C, the model of state B2 was rigid-body fitted into the density. The clearly invisible region in the pre-rRNA was removed. The further matured h41 and h42 pre-18S rRNA and two more r-proteins, eS19 and eS27, were homology built based on the yeast ribosome crystal structure (PDB ID: 4U4R).

Maps and models were visualized and figures created with the PyMOL Molecular Graphics System (Version 1.7.4, Schrödinger, LLC) and ChimeraX ([Goddard et al., 2018](#)).

Figure Legends

Figure 1. Reconstitution of the Thermophilic Kre33–Enp2–Bfr2–Lcp5 and Noc4–Nop14–Emg12–Rrp12–Enp1 Modules and Cryo-EM Analysis of the Thermophilic 90S Particles

(A) The thermophilic Kre33–Enp2–Bfr2–Lcp5 module was biochemically reconstituted by overexpressing the recombinant thermophilic proteins in *Saccharomyces cerevisiae* under control of the *GAL1–10* promoter. The assembly factor *ctBfr2* was N-terminally tagged with ProtA-TEV, whereas *ctEnp2* was C-terminally tagged with Flag for subsequent tandem affinity purification. The eluates from that step were separated by SDS-PAGE followed by Coomassie blue staining. (B) An analogous approach was applied for the Noc4–Nop14–Emg1–Rrp12–Enp1 module, with *ctRrp12*-TEV-ProtA as first bait and *ctEnp1*-Flag as second. The pentameric protein complex was further separated on a 10–40% sucrose gradient. (C) SDS-PAGE of the *ctKre33*–*ctNoc4* 90S particle isolated using split-tag affinity purification of a *Chaetomium thermophilum* strain transformed with *ctKre33*-TEV-ProtA and *ctNoc4*-Flag constructs. The final eluate was analyzed by SDS-PAGE and Coomassie staining and a molecular weight marker is also shown. Bands identified by mass spectrometry are labeled on the right. For a complete list of all identified 90S factors (see [Table S1](#), sheet 1). (D) Cryo-EM structure of the *ct90S* pre-ribosome (state B1) presented in a cartoon representation in two orientations, with the *ctKre33* and *ctNoc4* modules shown in the indicated color code.

Figure 2. The Thermophilic 90S Cryo-EM Reveals the Molecular Organization of the Kre33 and Noc4 Modules

(A, C) The improved 90S cryo-EM map (State B1) with members of the Kre33–Enp2–Bfr2–Lcp5 module and Noc4–Nop14–Emg1–Rrp12–Enp1 module highlighted. Note that for Bfr2 only the C-terminus could be assigned, whereas Enp2 lacks parts of the C-terminus and Lcp5 lacks the N-terminus. The Rrp12 density is shown in different control levels. (B) The constructed models of the members of the Kre33–Enp2–Bfr2–Lcp5 module and part of the GTPase Bms1 that contacts Kre33 in color-coded ribbon representation. (C) Models for Noc4–

Nop14–Emg1–Rrp12–Enp1 module organized around rRNA helix h32-34. A poly-Ala model is provided for Rrp12 as a place holder.

Figure 3. Sequential Incorporation of the four 18S rRNA domains into the 90S Pre-ribosome.

(A) The cryo-EM reconstructions of six different 90S pre-ribosomal states are shown as color coded densities. Their temporal order is indicated by arrows in between the names. The top and middle row shows the six states in two different views (top or side view), the bottom row illustrates the increasing completeness of sequential incorporation of the four 18S rRNA domains into the 90S pre-ribosome. Names, average resolution and changes in protein composition are stated. Density of Utp-C complex in state a is shown at different contour level.

Figure 4. The EM States B2 and C of the *ct90S* Particle Give Insight into the Successive Incorporation of the Ribosomal Proteins eS27 and eS19

(A) Color labelled densities of *ct90S* developing from state B2 (left) to state C (right) are shown. Whereas the ribosomal protein eS27 is absent in state B2, in state C eS27 stabilizes the UTP-C complex (Utp22 and Rrp7) on the central domain of the pre-18S rRNA. (B) A ribbon representation of the *ct90S* h41-h42 region in the body of the *ct90S* particle. These rRNA helices are kept immature by Utp30 in state B2 (left), but already adopt the mature conformation in state C in association with eS19 (right).

Figure 5. *Ex vivo* Purification of the Kre33–Enp2–Bfr2–Lcp5 Module from *Sacharomyces cerevisiae*

(A) In yeast, endogenous Kre33, Bfr2, and Enp2 were C-terminally tagged with Flag-TEV-ProtA, whereas Lcp5 was N-terminally tagged with ProtA-TEV-Flag and all were purified using tandem affinity purification (lanes 2, 4, 6, 8). The eluates were compared with a purification of Utp10-FTpA (lanes 1, 3, 5, 7) on a Coomassie-stained 4–12% gradient SDS-PAGE gel. To analyze whether multiple copies of the assembly factors were present in the purified particle, a plasmid-based GFP-tagged copy was co-expressed and analyzed by western blotting

using anti-GFP antibodies (lower panel). Co-purification with Utp10-FTpA indicates a functional association of the GFP-tagged protein with 90S particles. (B) Enp1-FTpA was purified from wildtype (lane 1) and Bfr2-, Enp2-, and Kre33-depleted situations (1 h auxin addition, lanes 2–4). Eluates were analyzed by 4–12% SDS-PAGE with Coomassie staining. (C) 90S particles purified via Utp10-FTpA from Bfr2, Enp2 or Kre33 depleted strains (1h auxin addition, lanes 2–4) were compared to non-depleted conditions (lane 1) on a 4–12% SDS-PAGE gel with Coomassie blue staining. (D) Semi-quantitative mass spectrometry was performed on eluates from the Utp-10 purifications. The IBAQ values (derived from Max Quant analysis) of each depleted eluate (blue, Bfr2; green, Enp2; red, Kre33) were divided by the values obtained for the wild-type control. The data were normalized for Utp6. The upper part of the diagram shows the fold of protein enrichment plotted from 1x (no enrichment) to 5x enrichment, the lower part shows the depletion from 1x to 35x in a linear scale.

Figure 6. Functional and Structural Characterization of the *kre33-1* Mutant

(A) Temperature-sensitive growth phenotype of *kre33-1* and associated suppressors. The indicated plasmid encoded Kre33 alleles (see plasmid table) were transformed into a Kre33 shuffle strain, shuffled on SDC+FOA and spotted in a 10x dilution series on YPD plates. 23 and 37 °C plates are shown after incubation for 3 days, and 30 and 35 °C plates are shown after 2 days. (B) Multiple sequence alignment of a Kre33 fragment (705-883aa) indicates the position and conservation of the mutated Kre33 amino acids. The indicated numbers correspond to the yeast Kre33. Sequences were aligned with Clustal Omega and Jalview. (C) The structure of *ctKre33* reveals its organization into domains and also the structural context of the *ctKre33* L790 residue, which is positioned in the C-terminal domain that mediates the homodimerization of Kre33.

Figure 7. Mutations in Kre33 Module and Krr1 Reveal the Link to 90S Biogenesis and Maturation

(A) Structure of the Kre33 module as revealed in the cryo-EM structure. Bfr2 C-terminal sequence (red) is in contact with the distal Kre33 copy (green), Enp2 β -propeller (blue) and the Krr1 C-terminal helix (orange). Amino acid borders indicate sequence regions according to the cryo-EM structure. (B) Structure-based mutational analysis of Bfr2. *Left panel:* wild-type and mutant versions of *BFR2* (inserted into plasmid pRS315) or empty pRS315 were transformed into the *bfr2 Δ* shuffle strain, and complementation was tested at 30° C on FOA plates (upper part). Strains selected on SDC+5-FOA plates were analyzed for their growth on YPD (lower part) at the indicated different temperatures. *bfr2 Δ C1*, aa 515-534 deleted; *bfr2 Δ C2*, aa 488-534 deleted, *bfr2 Δ C3*, aa 432-534 deleted. *Middle panel:* Kre33 module member Enp2 was genomically tagged with Flag-TEV-ProtA in the the *BFR* wild-type and *bfr2 Δ C2* strains, before affinity-purification of the indicated bait proteins was performed. Shown are the final eluates analyzed by SDS-PAGE and Coomassie staining. *Right panel:* Bfr2-FTpA or Bfr2 Δ C2-FTpA (constructs inserted into pRS315) were transformed into the *bfr2 Δ* shuffle strain and cells were selected on SDC+5-FOA for loss of the *BFR2* (inserted into the *URA3*-containing plasmid pRS316). The indicated bait proteins were affinity-purified and analyzed by SDS-PAGE and Coomassie staining. (C) Structure-based mutation of the Krr1 C-terminal helix and its genetic link to *enp2 Δ C*. *Left panel:* *KRR1* wild-type and *krr1 Δ C* mutant alleles (inserted into plasmid pRS315) or empty pRS315 plasmid were transformed into the *krr1 Δ* *ENP2* shuffle or *krr1 Δ* *enp2 Δ C* shuffle strains and complementation was tested by growth on 5-FOA plates at 30° C, or after shuffling on YPD-plates at different temperatures. *Middle panel:* Enp2-FTpA and Enp2 Δ C-FTpA (inserted into pRS315) were transformed together with wild-type *KRR1* or *krr1 Δ C* mutant alleles into the *krr1 Δ -enp2 Δ* double shuffle strain, before after shuffling on 5-FOA growing colonies were used for affinity-purification of chromosomally integrated bait constructs. *Right panel:* UTP-A factor Utp10 was C-terminally tagged with Flag-TEV-ProtA and affinity purified from either the *KRR1 enp2 Δ C* or *krr1 Δ C enp2 Δ C* strains (left panel). Growth was analyzed by plating cells in 10-fold serial dilution on the indicated plates, followed by incubation for 2 days at the indicated

temperatures. Bait proteins were isolated from cultures harvested in the mid-log growth phase, grown at 30° or shifted to 23°C for 10h, before Flag eluates obtained by by tandem affinity purification were analyzed by 4-12% gradient SDS-PAGE and Coomassie staining. Bait proteins are indicated with an asterix and labeled bands were identified by mass spectrometry.

Supplemental Figures

Figure S1. Interaction Network of the Thermophilic Kre33–Enp2–Bfr2–Lcp5 and Rrp12–Enp1–Nop14–Noc4–Emg1 Modules

(A) All possible yeast two-hybrid interactions for the Kre33–Enp2–Bfr2–Lcp5 module (right panel) and Noc4–Nop14–Emg1–Rrp12–Enp1 module (left panel) were analyzed using a systematic approach. All assembly factors from *Chaetomium thermophilum* were N-terminally tagged, except for *ctEnp2* and *ctRrp12*, which were C-terminally tagged, because N-terminal tagging affected their functionality. These plasmids (see also Plasmid Table) were transformed into yeast strain PJ69-4. Growth analysis is shown after incubation for 4 days at 30 °C on SDC–Leu–Trp (left) and SDC–Trp–Leu–His+2 mM 3AT (Kre33 module right) or on SDC–Trp–Leu–His+1 mM 3-AT (Noc4 module right). (B) The interactions within the Kre33–Enp2–Bfr2–Lcp5 module were biochemically reconstituted (upper panel). The indicated thermophilic proteins were tagged with either ProtA-TEV or Flag epitope and overexpressed in *Saccharomyces cerevisiae* under the control of a Gal1–10 promoter. The eluates of the tandem affinity purification were separated on SDS-PAGE and stained with Coomassie blue. The analogous approach was applied for members of the Noc4–Nop14–Emg1–Rrp12–Enp1 module (lower panel). For *ctRrp12*, the truncated *ctRrp12ΔC* (1–1039 aa) construct was used due to its superior biochemical properties. (C) Association of *scRrp12ΔC* with 90S pre-ribosomes. 90S pre-ribosomal particles were affinity purified from the wildtype and an *scRrp12ΔC* mutant using Utp18-FTpA. Eluates were analyzed by 4–12% gradient SDS-PAGE and Coomassie blue staining (upper panel). The positions of *scRrp12* and *scRrp12ΔC* were confirmed by mass spectrometry. Growth analysis of *Saccharomyces cerevisiae* wild-type *RRP12* and a *rrp12ΔC* mutant on YPD plates at the indicated temperatures (lower panel). The plasmid-based *RRP12* alleles were transformed into a *rrp12Δ* shuffle strain, and grown on SDC+5-FOA, before 10-fold dilutions were spotted onto YPD plates and incubated for 2 days.

Figure S2. Classification of Different 90S cryo-EM Intermediates

(A) Cryo-EM data processing and classification of the *ct*90S pre-ribosome dataset with final volumes highlighted in colours. An overall resolution average is given below the EM-maps (where C_x indicates class x). (B) The gold-standard fourier shell correlation (FSC) curves of the six different states is shown. (C) The FSC plot of state B1 model against the cryo-EM map. (D) The local resolution distribution was estimated by using Relion from the overall refinement (left) and two focussed refinements (middle and right) ranging from approximately 3 Å (dark blue) to 7 Å (red). For intermediate resolution see refer to scale bars.

Figure S3. *In vivo* Analysis of the Kre33 Module in *Saccharomyces cerevisiae*

(A) Sucrose gradient analysis of affinity-purified Kre33–Enp2–Bfr2–Lcp5 module derived from the yeast *Saccharomyces cerevisiae*. Enp2-FTpA was purified from a wild-type background and subsequently analyzed by sucrose gradient centrifugation (10–50%). Fractions were analyzed by SDS-PAGE and Coomassie blue staining. (B) The same analysis like in (A) was performed with a Kre33-FTpA affinity-purified eluate. (C) Selected lanes of fraction 2 and 8 depicted under (A) were cut out and displayed shown side-by-side with fraction 7 of panel B. The position of the Kre33–Enp–Bfr2–Lcp5 module components is indicated. (D, E) *In vivo* interdependence of the yeast Kre33–Enp2–Bfr2–Lcp5 module upon depletion of individual factors. An *ENP1*-FTpA, *osTIR1* strain (D) or *UTP10*-FTpA, *osTIR1* strain (E) was used to tag *BFR2*, *ENP2* and *KRE33* with an HA-aid tag. The derived strains were plated on YPD and YPD+Auxin (0.5 mM) and incubated for 2 days at 30 °C. The depletion efficiency upon auxin addition was monitored by western blot analysis (anti-HA), whereas bait proteins Enp1 or Utp10 were detected with anti-protA antibodies.

Figure S4. The *kre33-1* Mutant Has a Reduced Association with Pre-ribosomes

(A) Deletion strains *kre33Δ* carrying pRS315-*KRE33*-FTpA or pRS315-*kre33-1* whole cell lysate supernatants were analyzed on a 10–50% sucrose gradient. The corresponding absorption profiles at 254 nm are shown, indicating the position of 40S, 60, 80S and polysomes. Western blot analysis was performed to determine the sedimentation behavior of the Kre33 protein. Note that the expression level of the mutant is lower at 37° C. (B) Whole cell lysate inputs used for gradient analysis (see A) were loaded onto the same gel to determine the differences in the protein levels. (C) Time-course of shifting the Kre33 wild-type and *kre33-1* mutant to the restrictive temperature. Levels of Kre33 wild-type and mutant protein upon shifting to 37 °C were determined by western blotting. Anti-Arc1 western detection was used as a loading control. (D) Plasmid-derived Kre33-FTpA (wt) and Kre33-1-FTpA (ts1) were expressed in a *kre33Δ* background and affinity-purified. The final eluates were analyzed by 4-12% SDS-PAGE and Coomassie blue staining.

Figure S5. Genetic Interactions between Members of the Kre33 Module and Krr1 and Multiple Sequence Alignments of Enp2 and Bfr2

(A) Double shuffle strains were transformed with a combination either wild-type and wildtype-single mutant alleles of Bfr2, Enp2, Krr1 and Kre33 and a pairwise combination of the mutant alleles generated during the course of this study. Gene variants inserted into plasmids pRS315 and pRS414 as well as strains are listed under Methods. Cells were selected on SDC+5-FOA, plated on YPD in 10-fold serial dilutions and it was incubated for 2 days at the indicated temperatures. (B) Multiple sequence alignment of the C-terminal end of Enp2 and amino acid position where the Enp2ΔC deletion has been generated. (C) Multiple sequence alignment of the C-terminal region of Bfr2. The positions of the Bfr2 C-terminal deletion mutants described in Figure 7 are indicated, as well as the meandering sequence seen in the cryo-EM structure (red bar). The alignments were generated using ClustalW and Jalview. *S.c. Saccharomyces cerevisiae*, *S.p. Schizosaccharomyces pombe*, *C.t. Chaetomium thermophilum*, *A.t. Arabidopsis thaliana*, *D.m. Drosophila melanogaster*, *M.m. Mus musculus*, *H.s. Homo sapiens*.

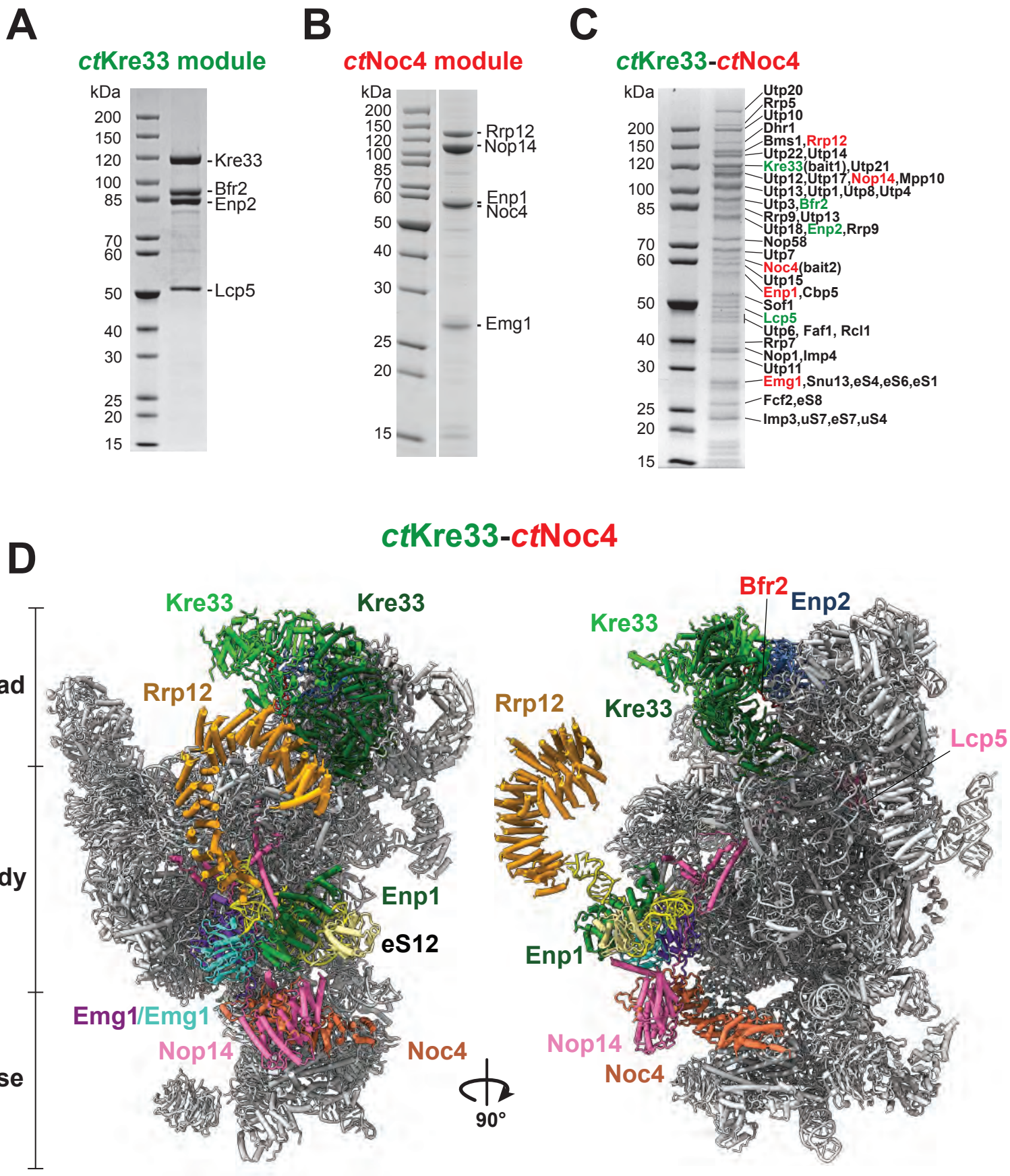


Figure 1

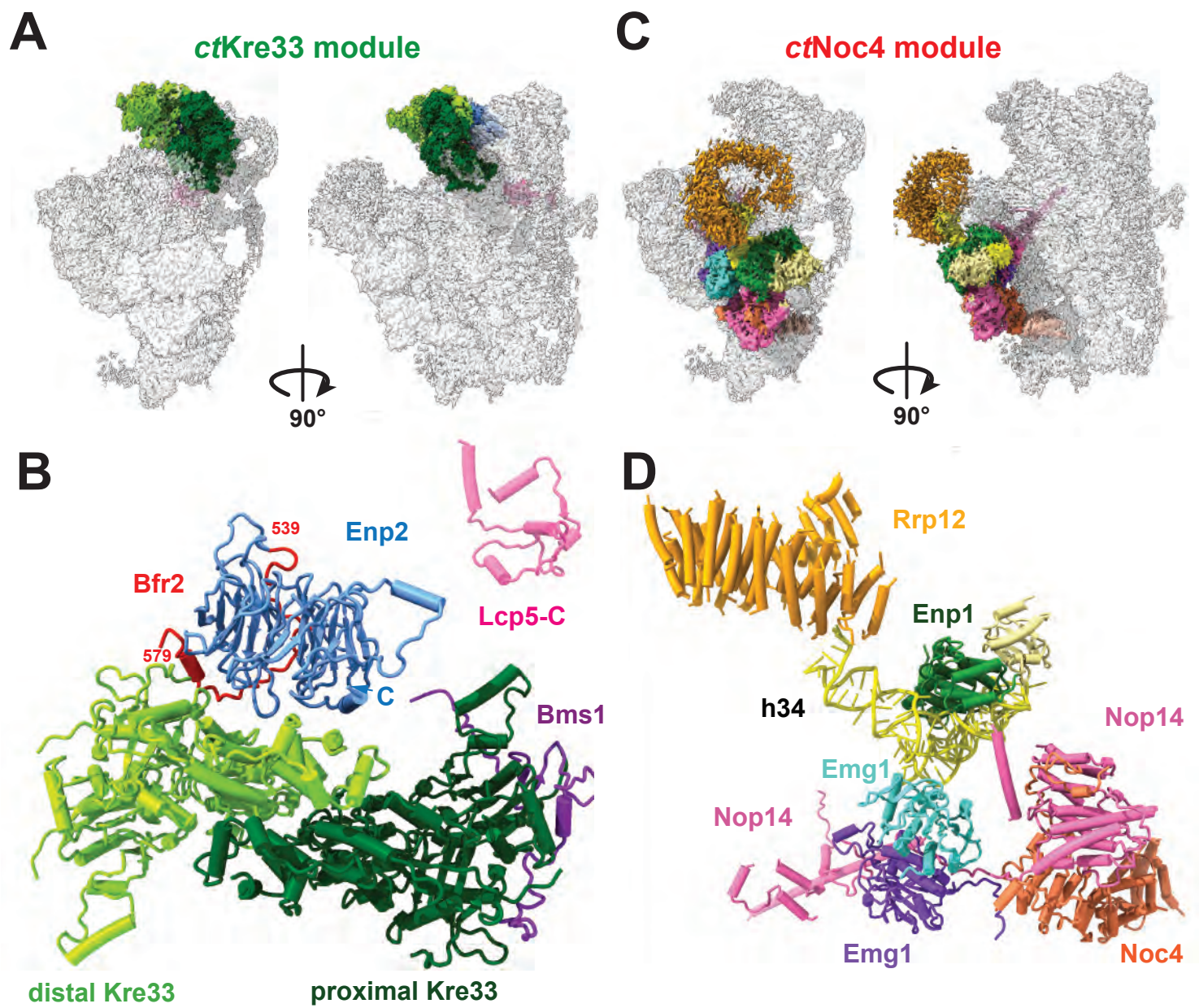


Figure 2

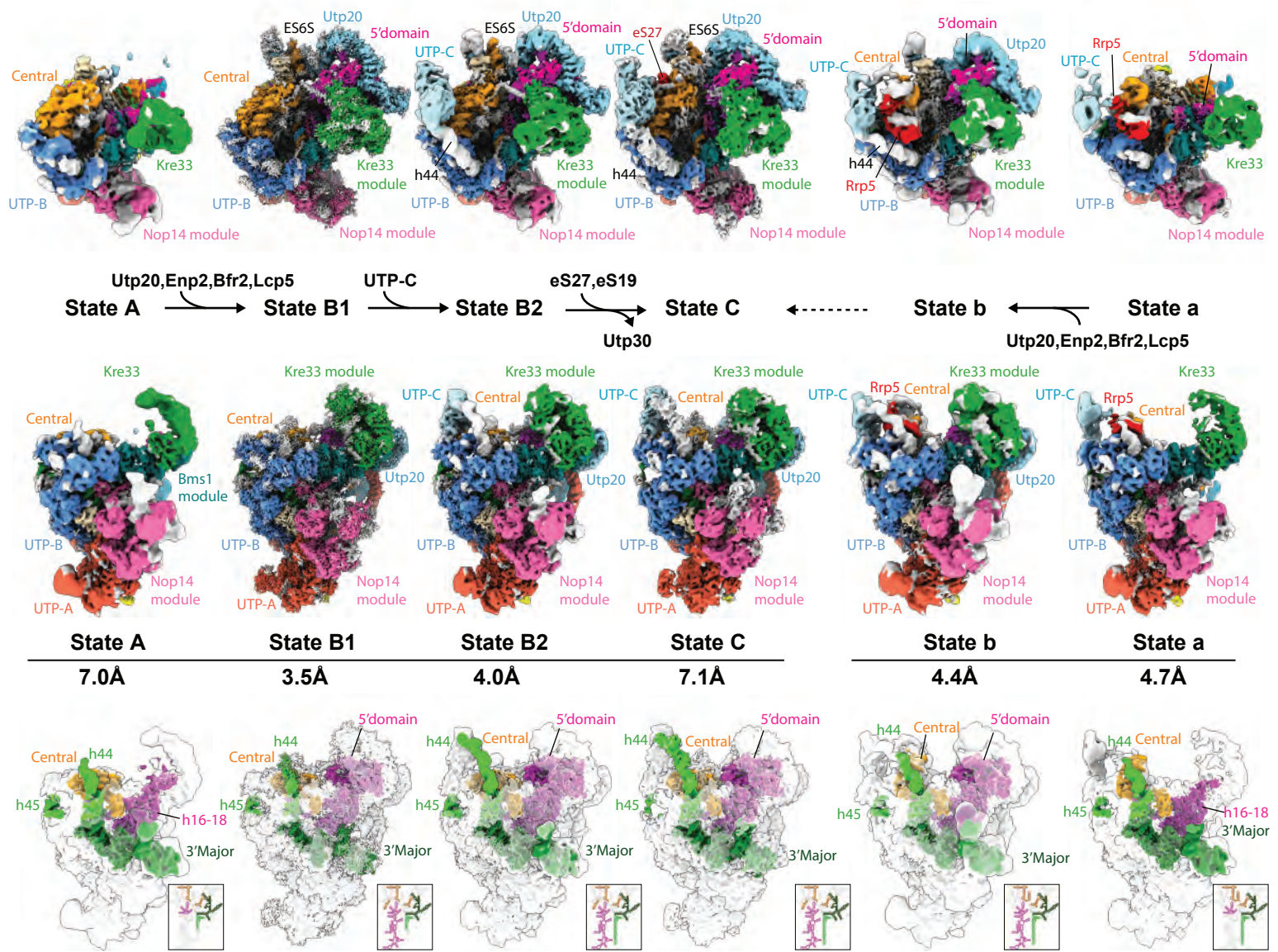


Figure 3

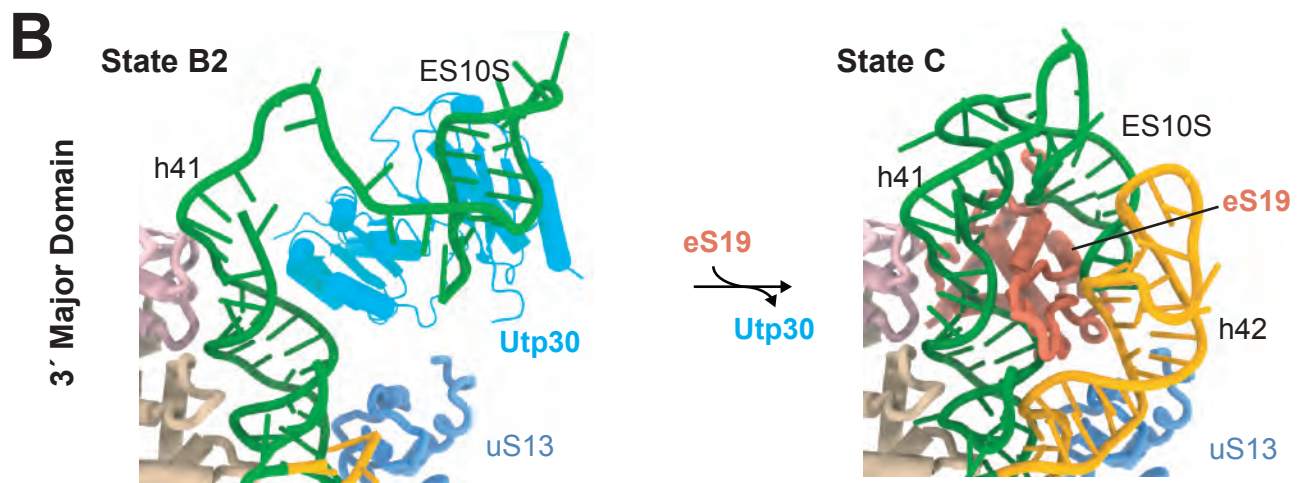
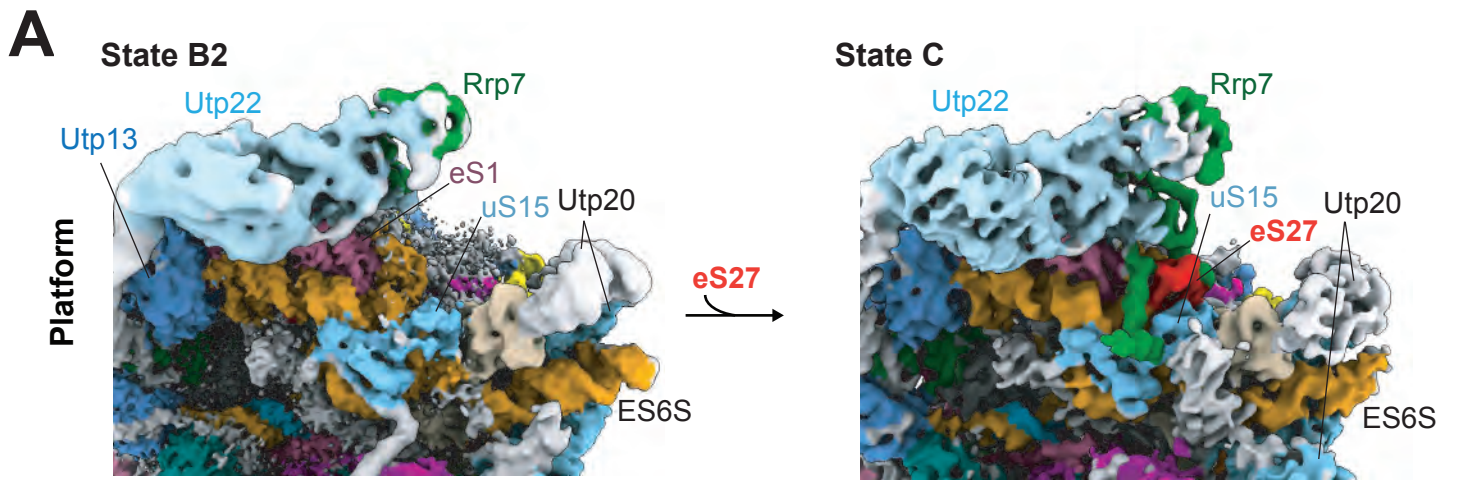


Figure 4

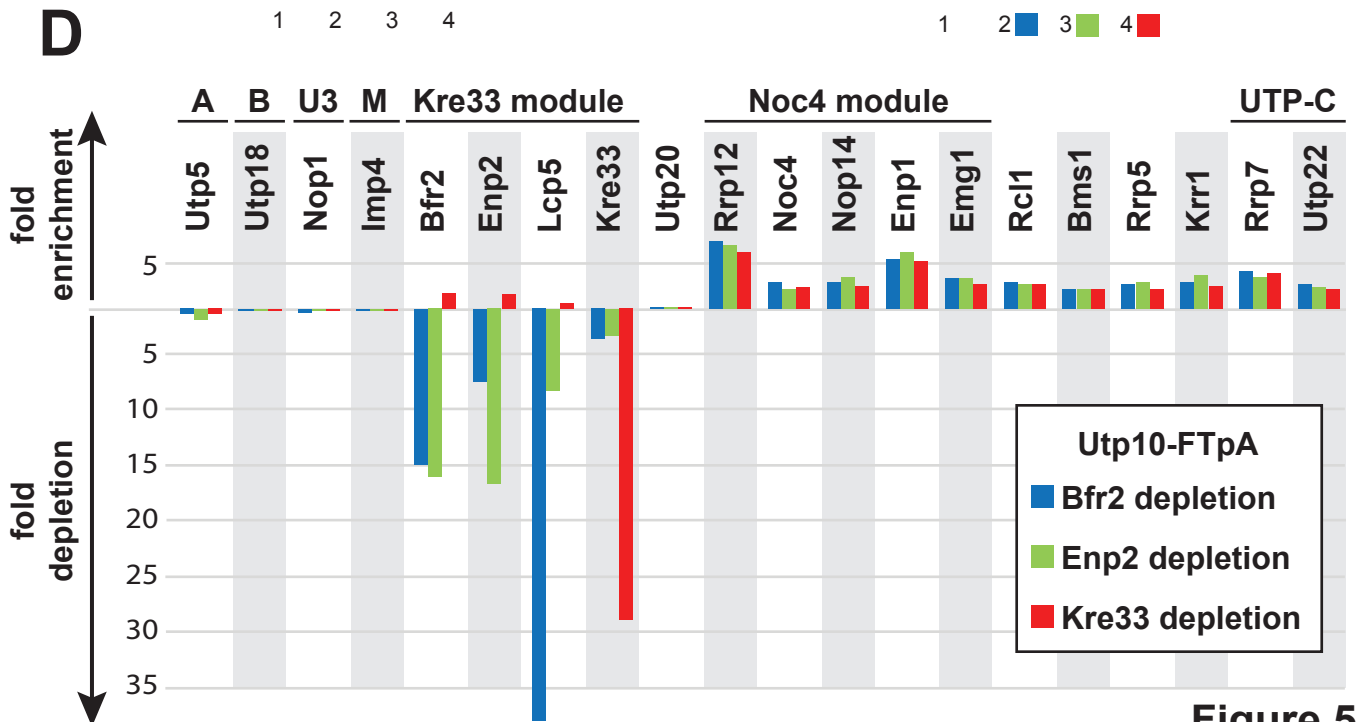
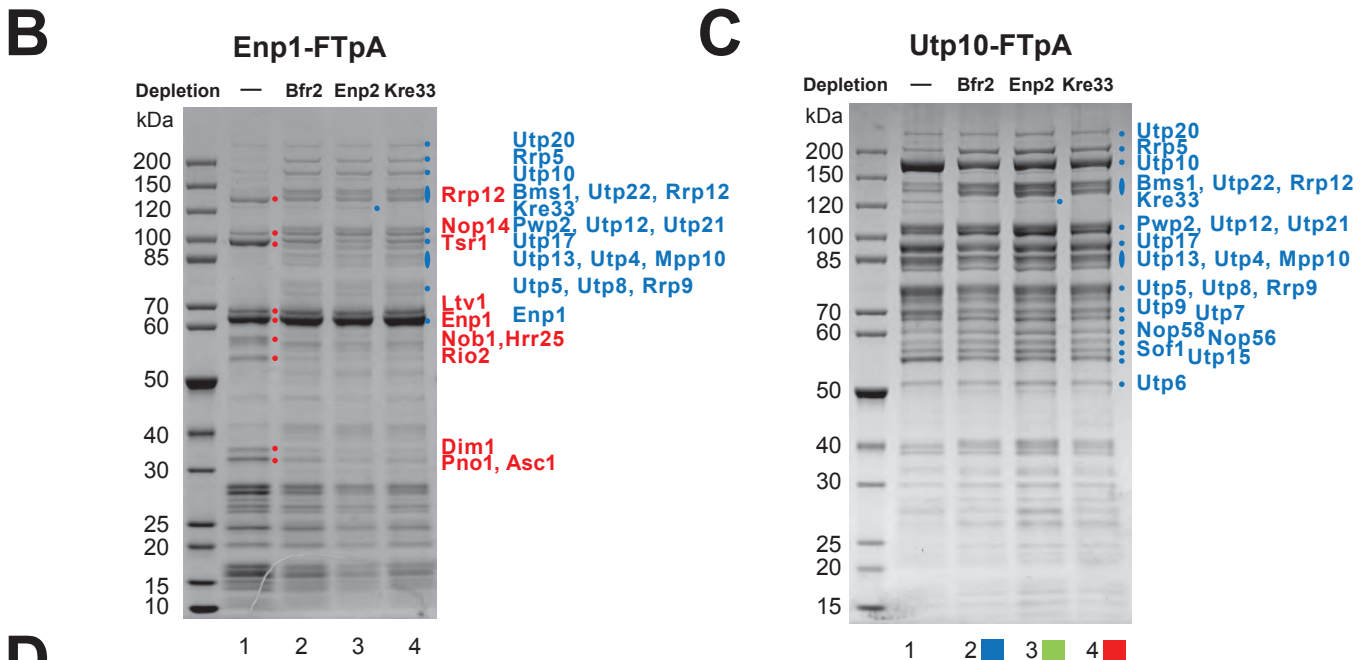
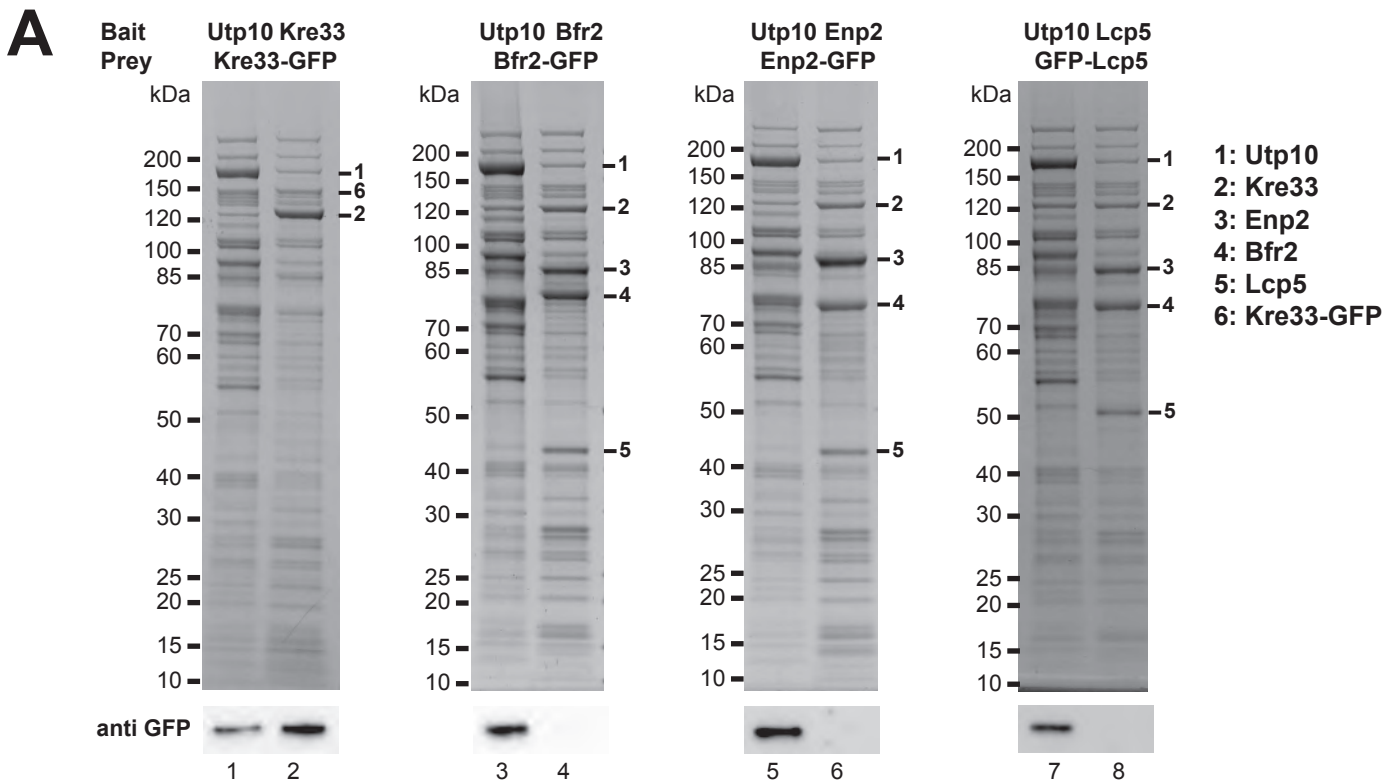
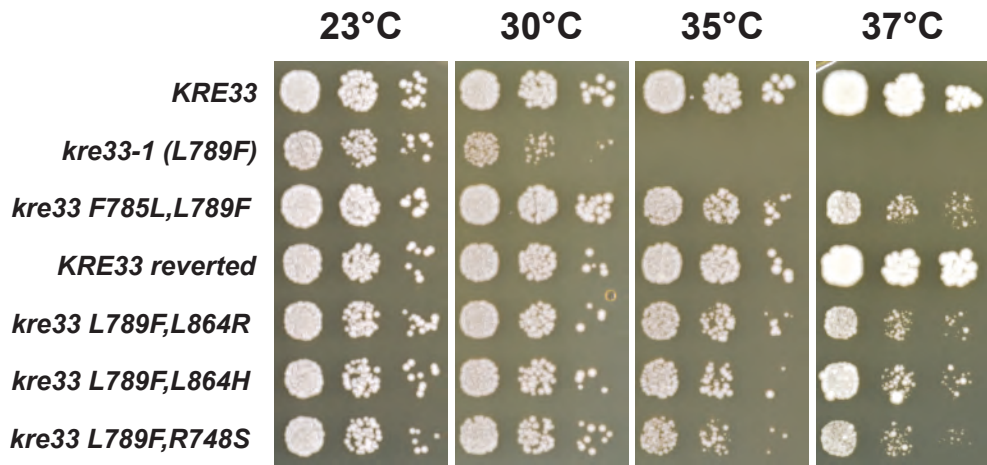
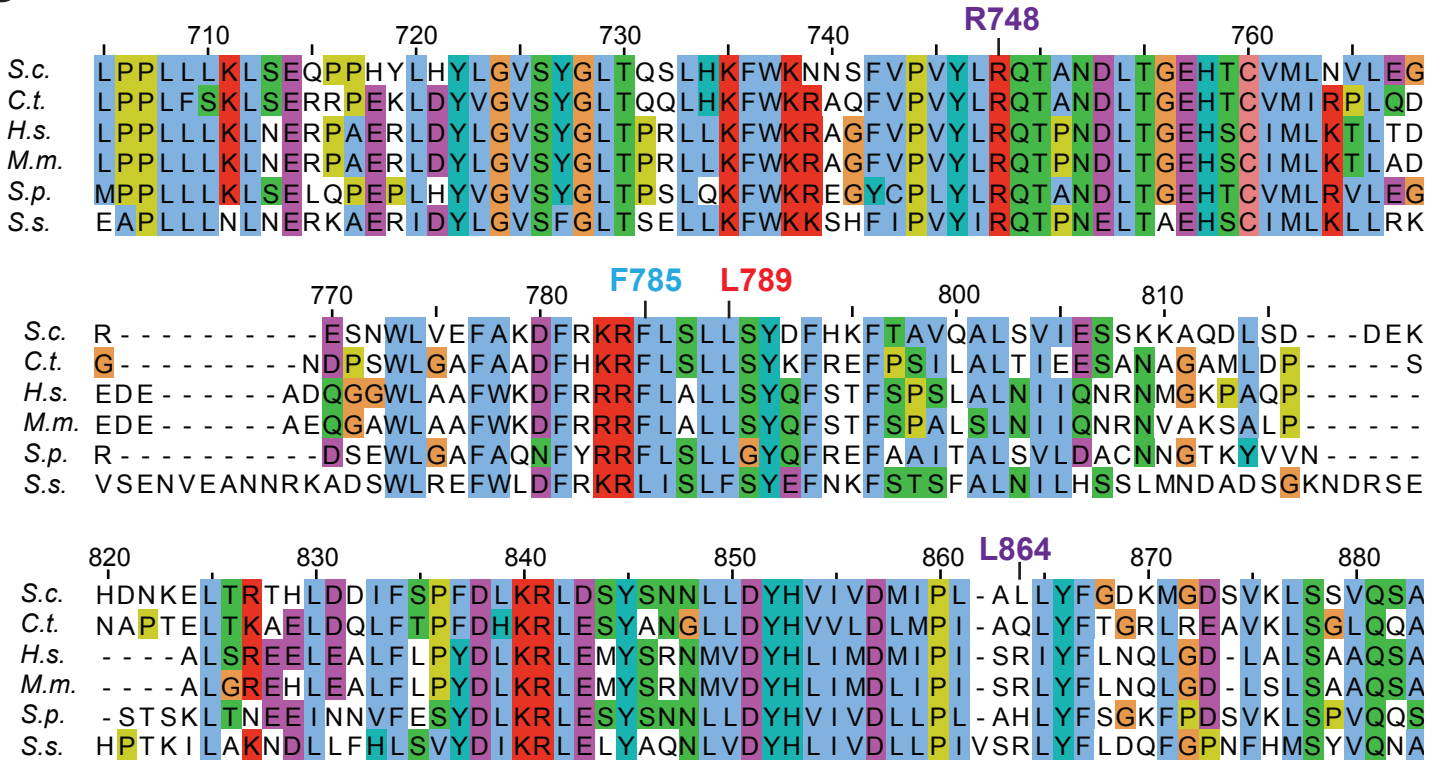
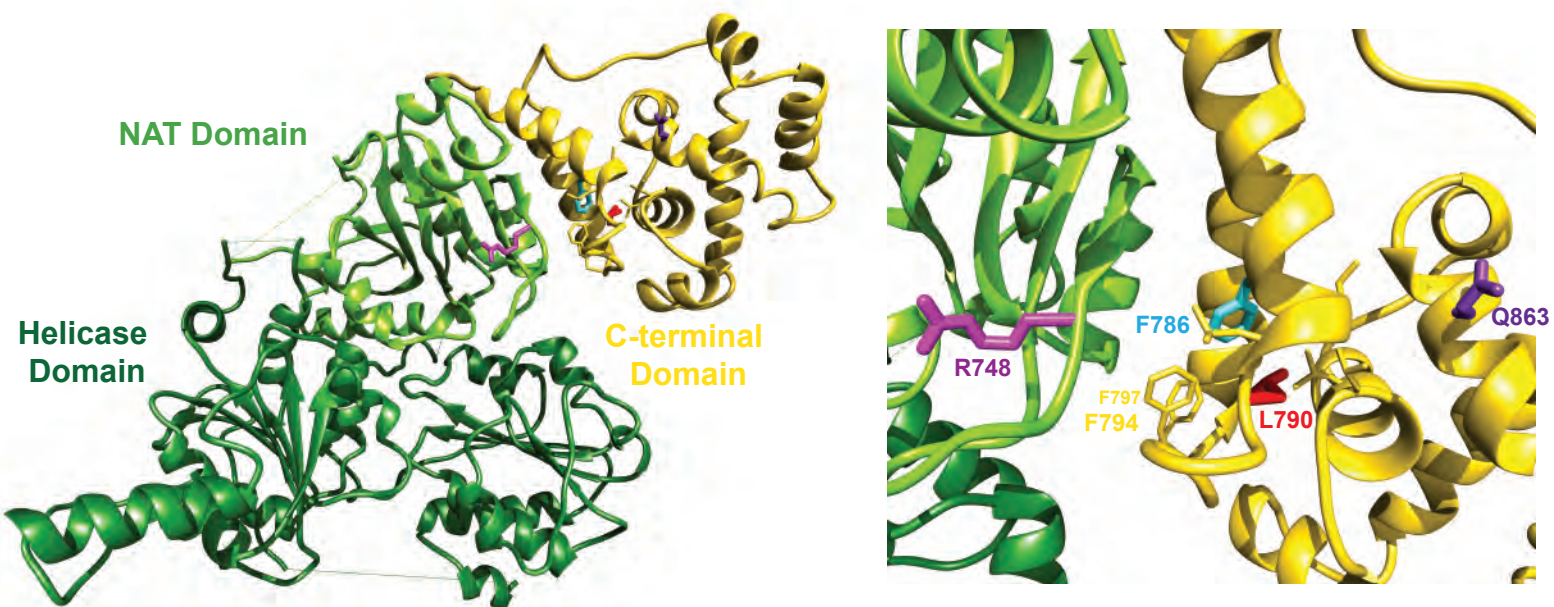
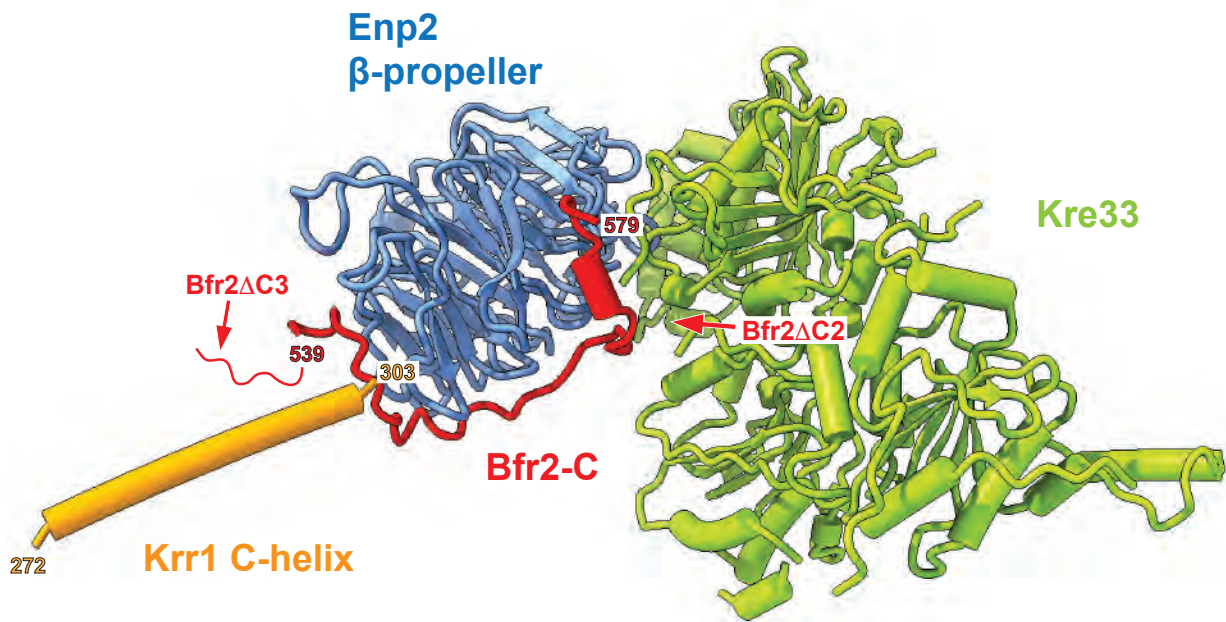
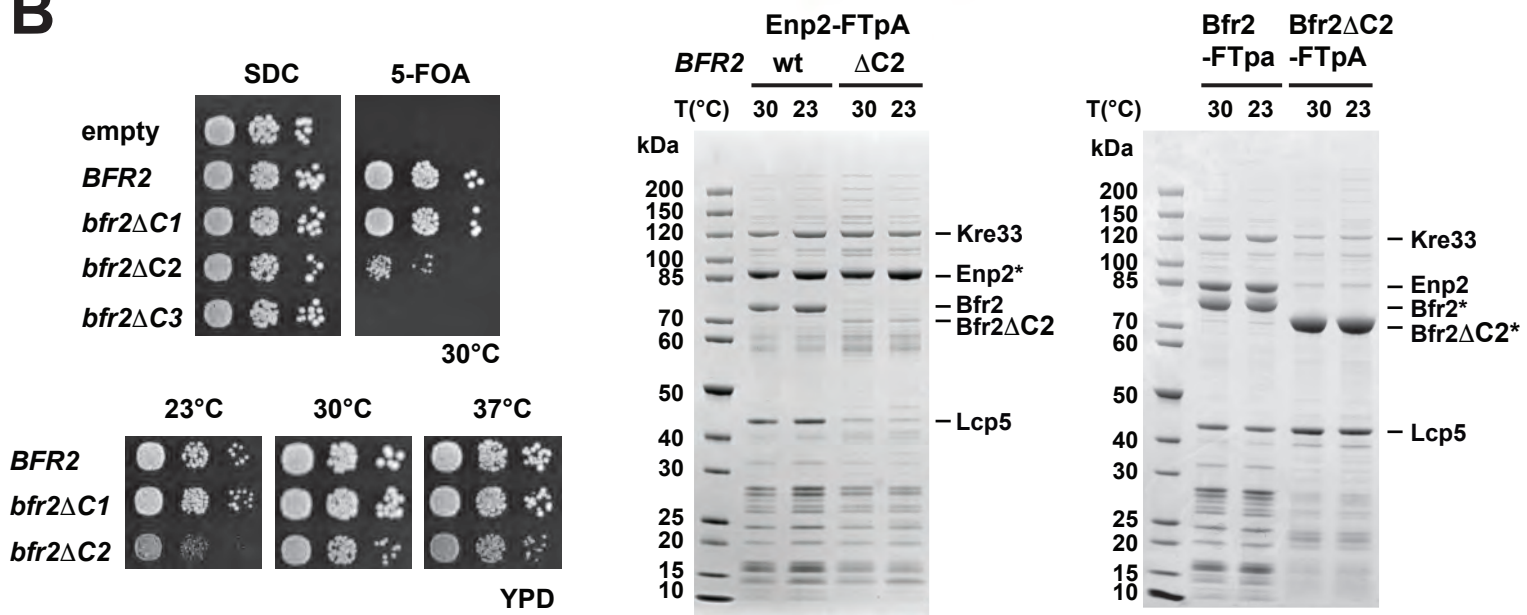
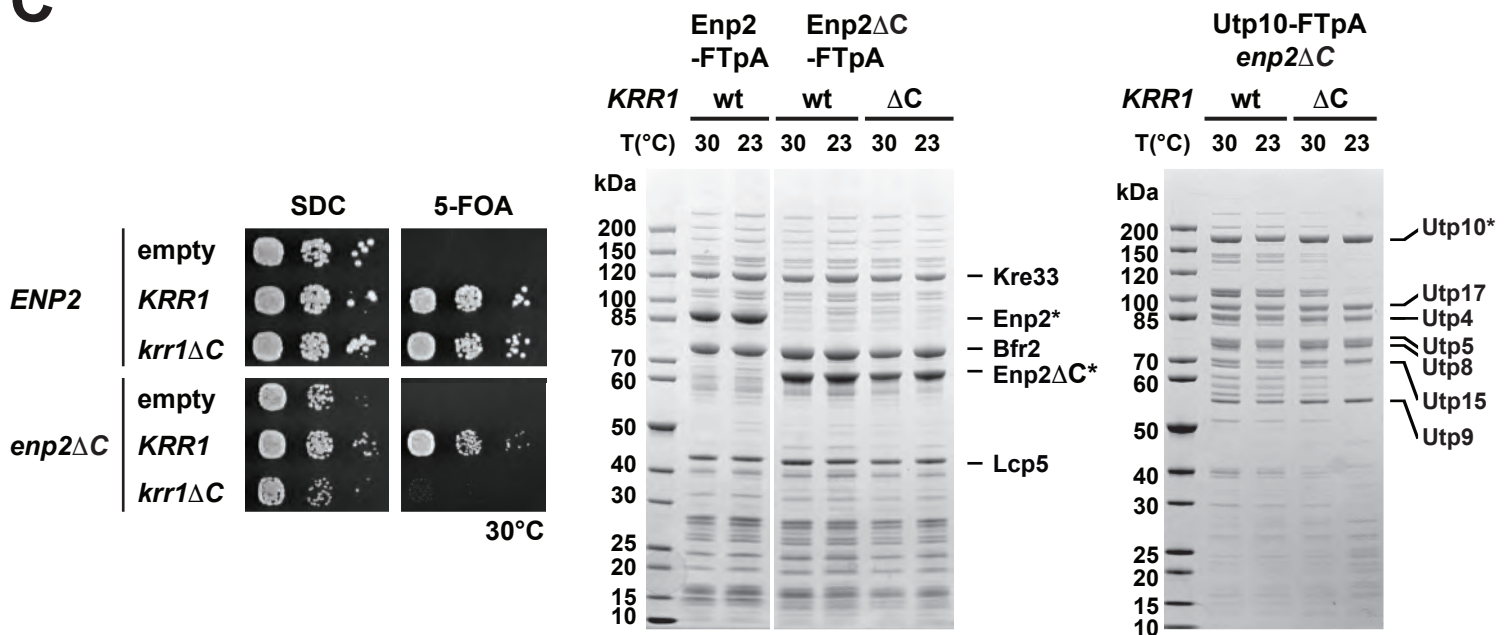


Figure 5

A**B****C****Figure 6**

A**B****C****Figure 7**

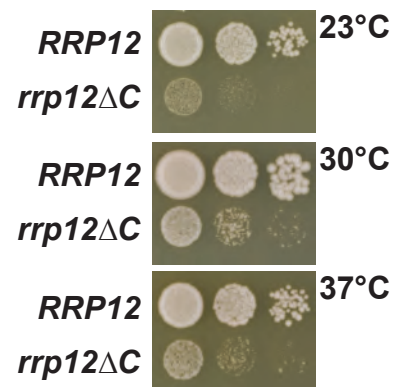
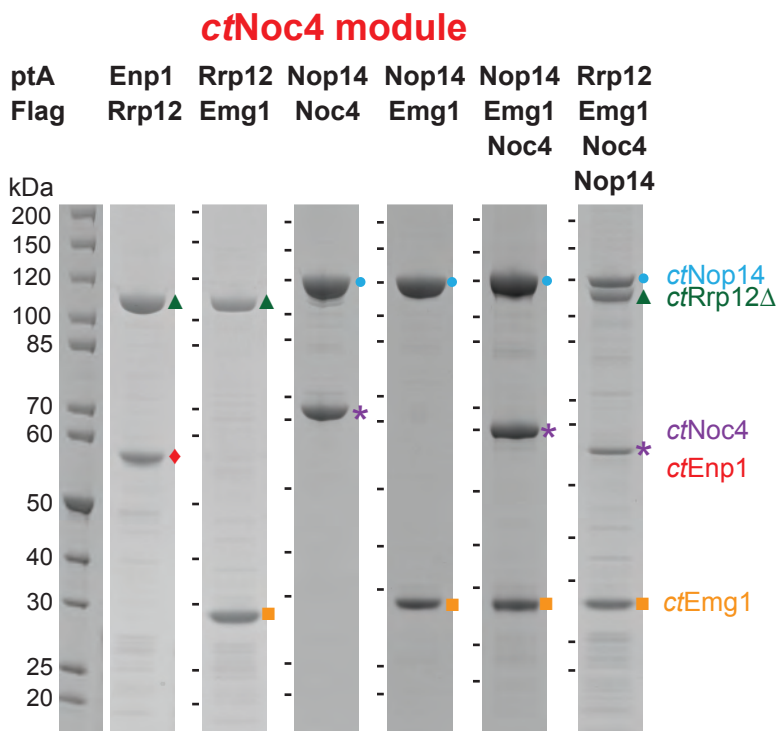
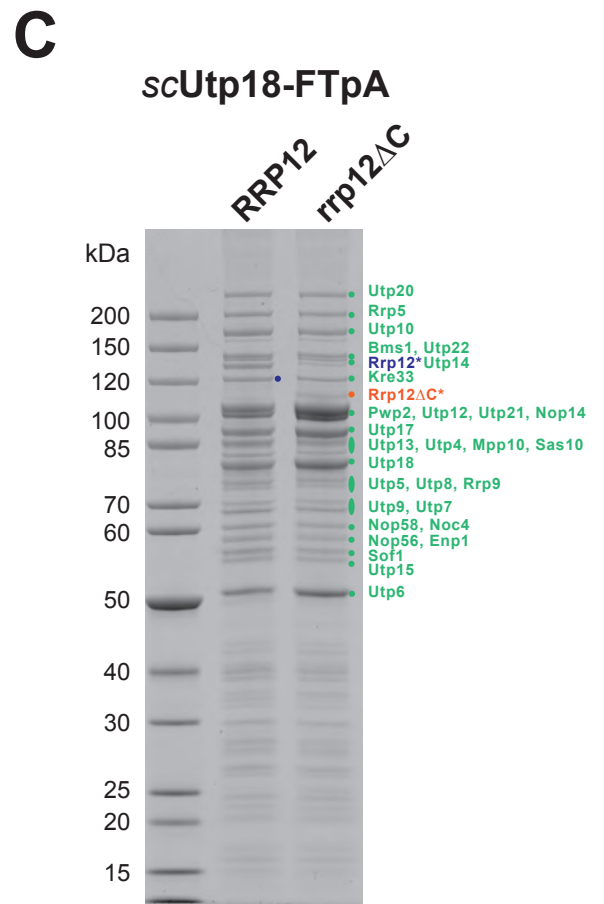
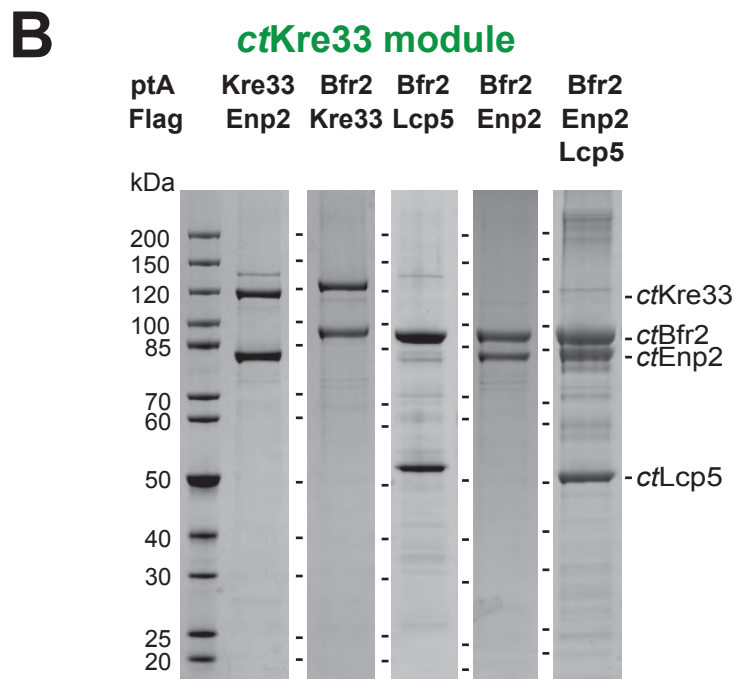
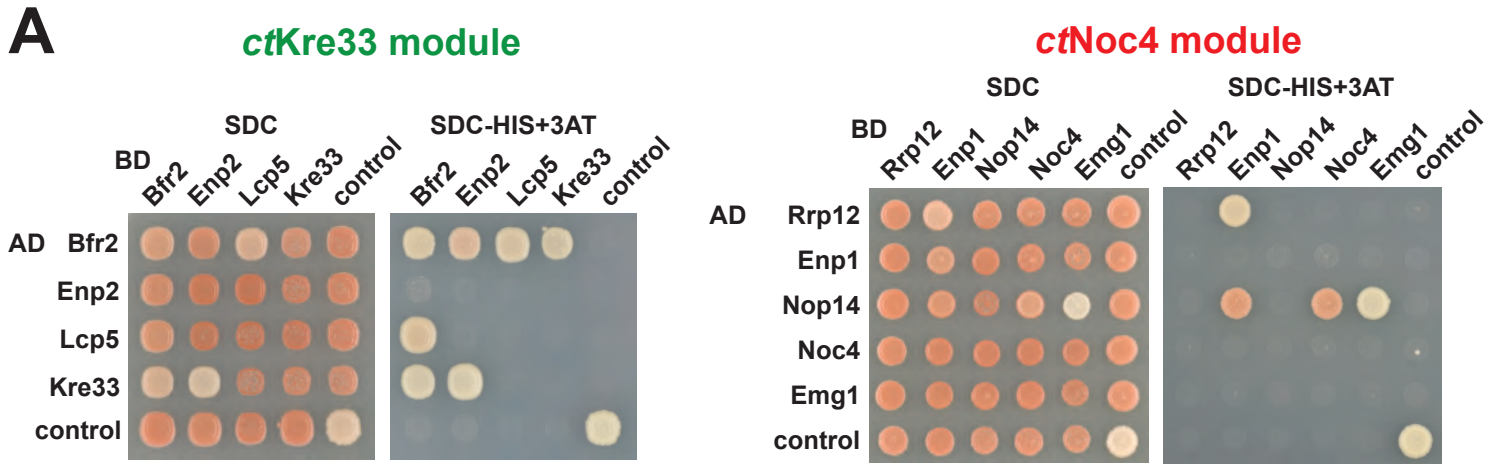
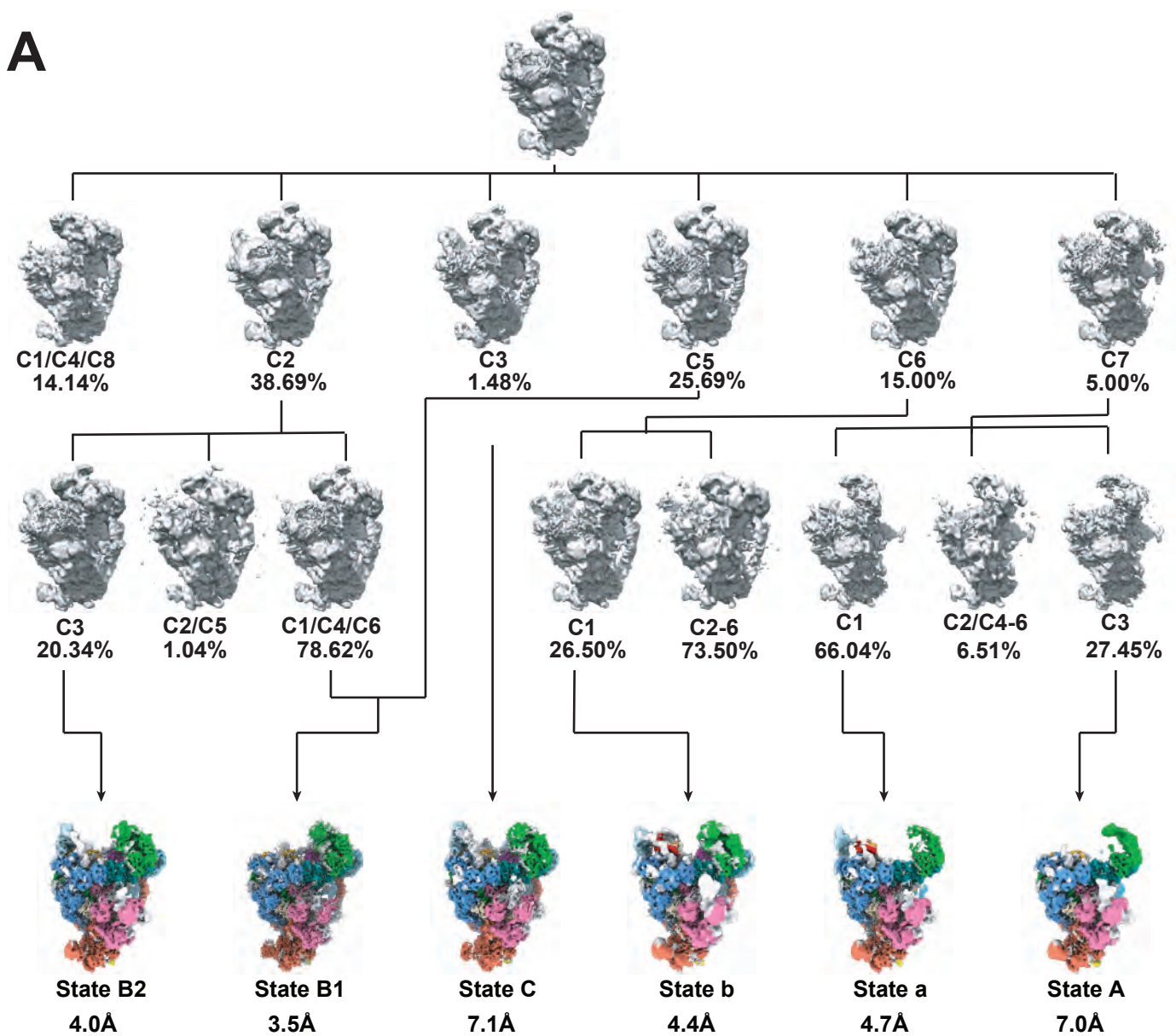
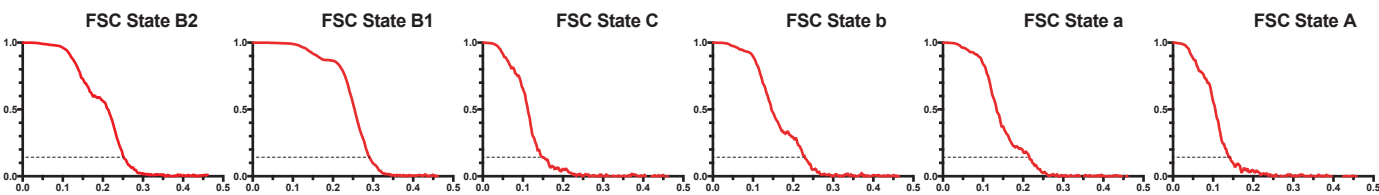
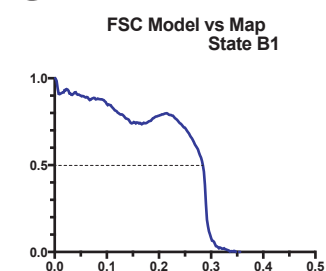
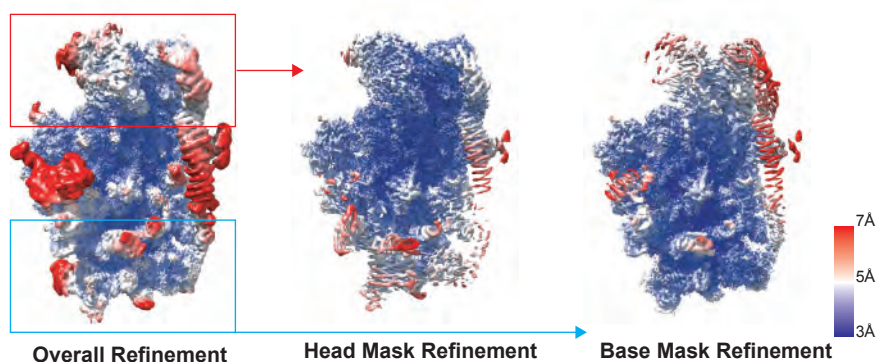


Figure S1

A**B****C****D****Figure S2**

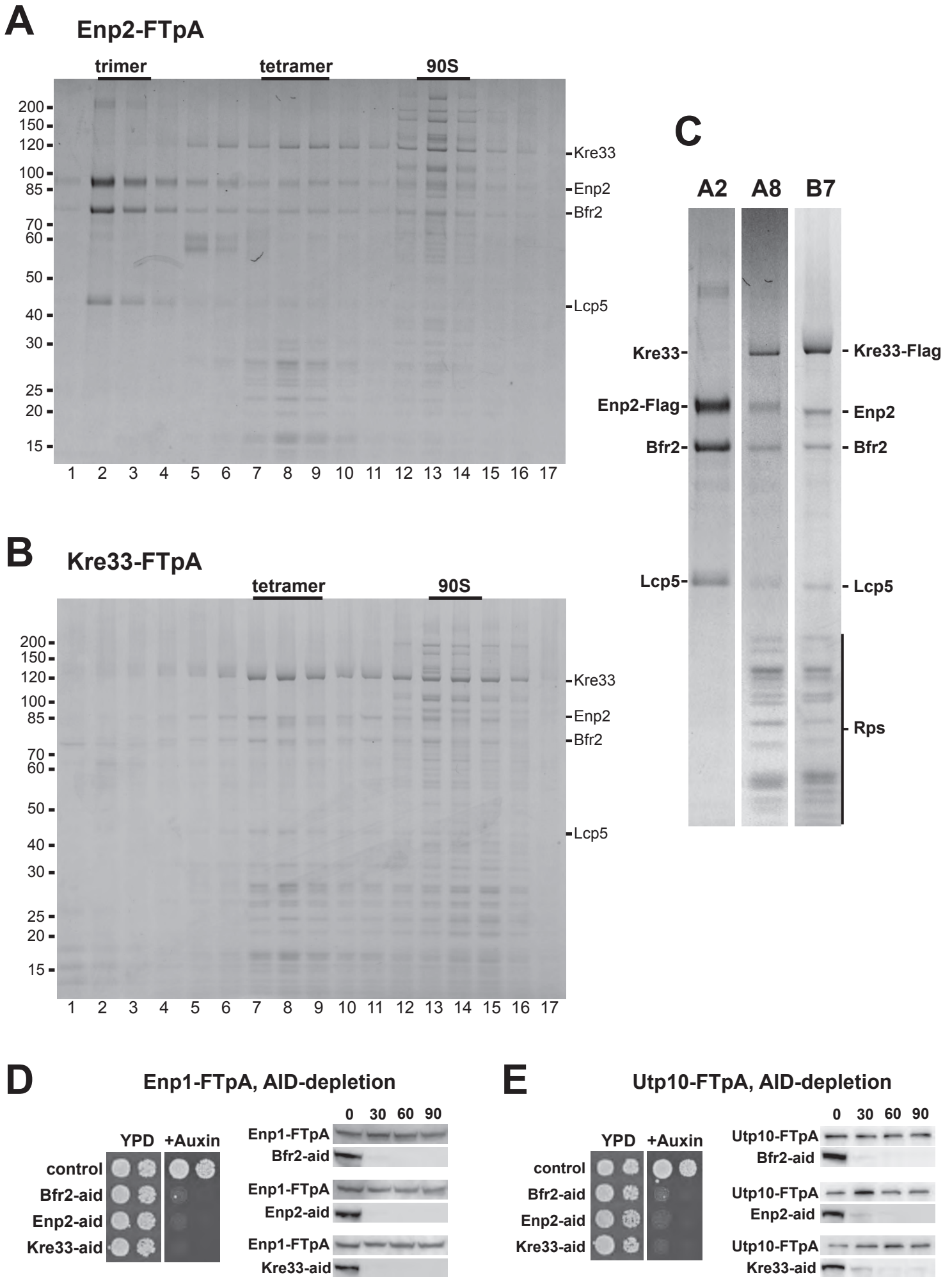


Figure S3

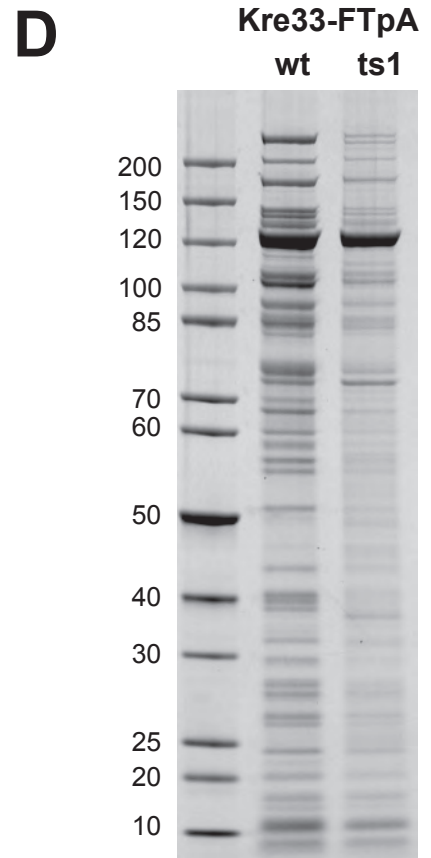
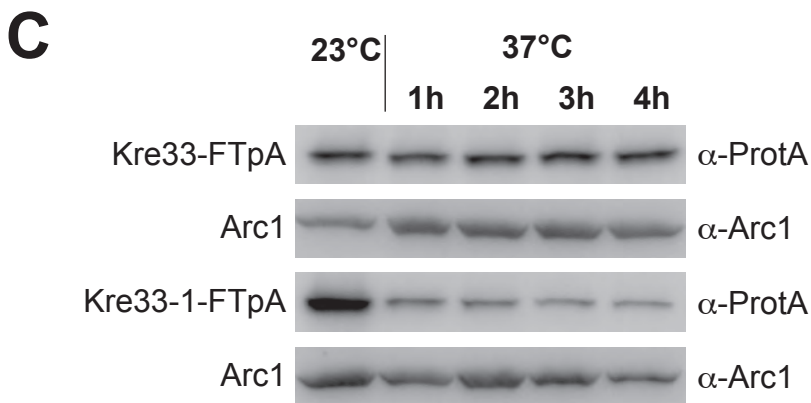
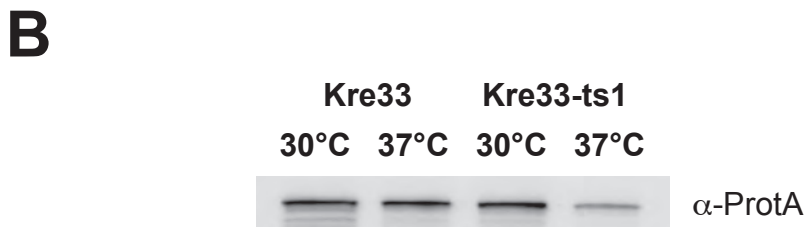
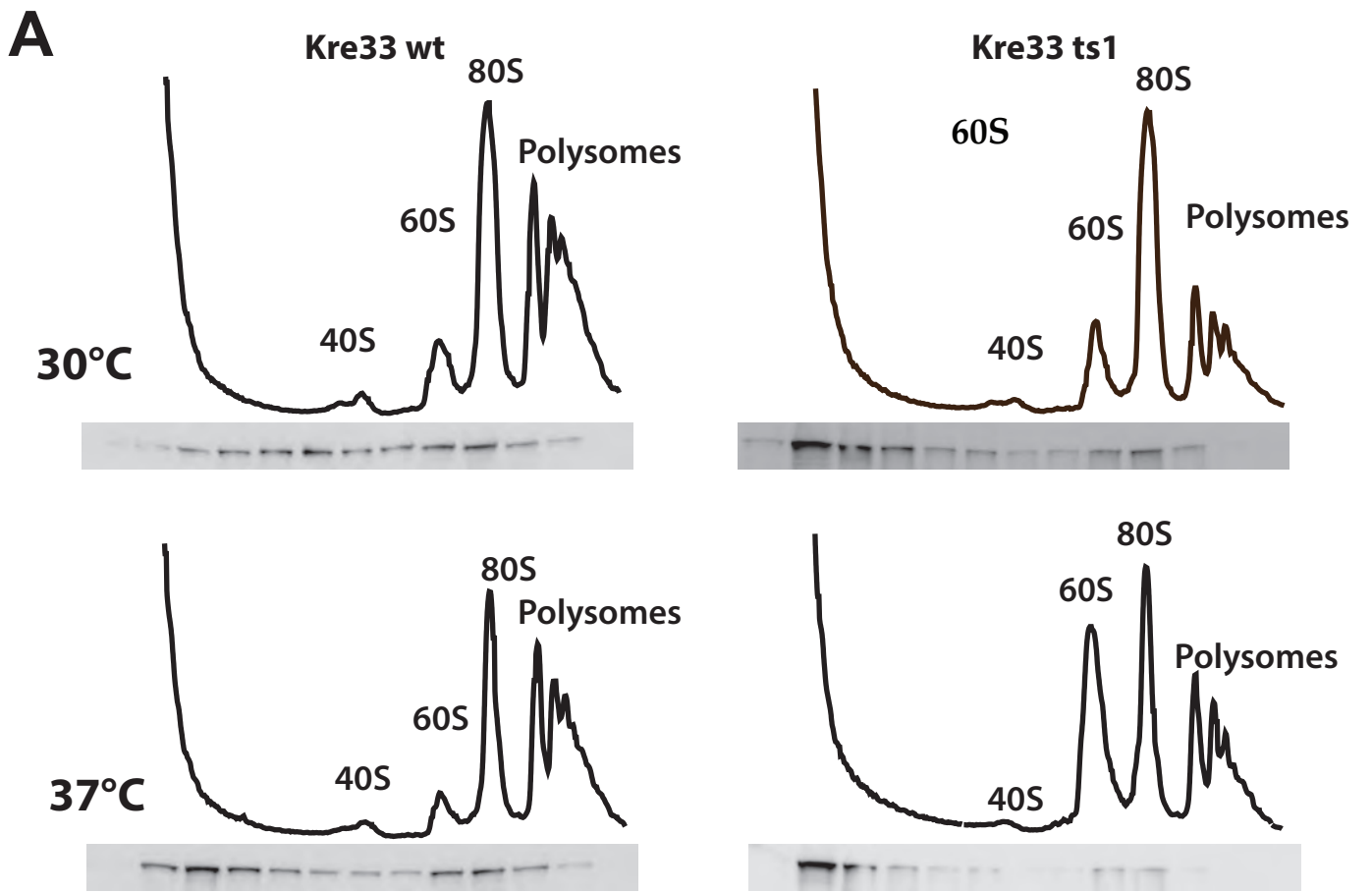


Figure S4

